PAPER

Check for updates

AntiCD44 antibody-conjugated gold nanoparticles for targeted photothermal therapy of endometriotic cells

Cristina Volpini, [a,b] Nora Bloise, [a,b] Claudio Casali, [c] Benedetta Albini, [d] Mattia Dominoni, [e,f] Fabio Barra, [g,h] Marco Biggiogera, [c] Pietro Galinetto, [d] Barbara Gardella, [e,f] Valerio Gaetano Vellone, [i,j] Simone Ferrero, *[k,l] Paolo Minzioni *[m] and Livia Visai *[a,b]

Endometriosis is a chronic gynecologic disease that needs newer and safer treatments. The proposed work aims to develop a nanosystem based on gold nanoparticles (AuNPs) to actively target human endometriosis CD44(+) cells and significantly reduce their viability by photothermal therapy (PTT). AuNPs stabilized by lipoic acid-Poly(ethylene glycol)-Maleimide (LA-PEG-Mal) (Au@P) were decorated with antiCD44 antibodies (Au@P_AbCD44) through maleimide chemistry. The physicochemical and biochemical approaches revealed the presence of the antibody on Au@P_AbCD44. The *in vitro* studies were conducted against overexpressing CD44 cells (12Z), low-expressing CD44 cells (HESC), and the normal fibroblast cell line (NIH-3T3). Following the internalization through the clathrin-mediated endocytosis, the PTT of the cell-internalized Au@P_AbCD44 was investigated using two distinct laser types, due to the differing Au@P's LSPR properties. Au@P_AbCD44 exhibited significant PTT efficacy against 12Z cells; however, GNS@P_AbCD44 required lower energy input compared to GNP@P_AbCD44. This enhanced performance is attributed to the LSPR-mediated photothermal conversion efficiency of GNS over GNPs.In both cases, the apoptotic pathway was selected by dying cells over necrotic cells. The results revealed a better photothermal ability of GNS@P_AbCD44 compared to GNP@P_AbCD44. Our findings highlight the clinical potential of gold nanostars as advanced photosensitizers for targeted photothermal therapy, offering a promising strategy for more effective and less invasive treatment of endometriosis.

1. Introduction

Endometriosis is an estrogen-sensitive disorder that leads to pelvic pain and infertility, impacting women and girls of reproductive age, with an occurrence rate between 6% and 10%. However, it may also be diagnosed during menopause.[1,2] Currently, the etiology of the disease remains unclear[3,4] as several molecular pathways are involved in the development of endometriosis: hormonal signaling, microenvironmental changes and abnormal immunological activity.[5] The evidence indicates that CD44 expression was observed in epithelial and stromal menstrual endometrial cells in women with endometriosis. It was postulated that this could be responsible for the increased binding capacity to peritoneal cells.[6,7] CD44 is a

[a]Molecular Medicine Department (DMM), Centre for Health Technologies (CHT), Unità di Ricerca (UdR) INSTM, Operative Unit (OU) of Interuniversity Center for the Promotion of the 3Rs Principles in Teaching and Research (Centro 3R), University of Pavia, 27100 Pavia, Italy. E-mail: jyfu@zju.edu.cn, livia.visai@unipv.it

[b]UOR6 Nanotechnology Laboratory, Department of Prevention and Rehabilitation in Occupational Medicine and Specialty Medicine, Istituti Clinici Scientifici Maugeri IRCCS, Via Maugeri 4, 27100 Pavia, Italy

[c]Laboratory of Cell Biology and Neurobiology, Department of Biology and Biotechnology "L. Spallanzani", University of Pavia, 27100 Pavia, Italy

[d]Dipartimento di Fisica, Università degli Studi di Pavia, Via Bassi 6, I-27100 Pavia, Italy

[e]Dipartimento di Scienze Cliniche, Chirurgiche, Diagnostiche e Pediatriche, Università di Pavia, Italy

[f]Ginecologia e ostetricia, iRCCS Fondazione Policlinico san matteo, Pavia, Italy

[g]Unit of Obstetrics and Gynaecology, IRCCS Ospedale Policlinico San Martino, Genoa, Italy

[h]Department of Health Sciences (DISSAL), University of Genoa, Genoa, Italy

[i]Dipartimento di Scienze Chirurgiche e Diagnostiche Integrate (DISC), Università di Genova, Italy

[j]UOC Anatomia Patologica, IRCCS Istituto Giannina Gaslini, Genova, Italy

[k]Department of Neurosciences, Rehabilitation, Ophthalmology, Genetics, Maternal and Child Health (DiNOGMI), University of Genova, Italy. E-mail: simone.ferrero@unige.it

[l]Unit of Obstetrics and Gynaecology, IRCCS AOU San Martino – IST, Genoa, Italy, Largo R. Benzi 10, 16132 Genoa, Italy

[m]Department of Electrical, Computer and Biomedical Engineering, Integrated Photonics Lab, University of Pavia, 27100 Pavia, Italy. E-mail: paolo.minzioni@unipv.it

transmembrane glycoprotein involved in cellular adhesion, leukocyte activation, and cell migration.[8] It is also involved in the interaction between other extracellular matrix components such as collagens, fibronectin, cytokines, chemokines, growth factors and metalloproteinases.[8] Due to the variability in the location and appearance of endometriotic lesions, diagnostic methods such as laparoscopy, transvaginal ultrasound (TVUS), and magnetic resonance imaging (MRI)[9] are insufficient, often resulting in diagnostic delays or misdiagnosis.[10] Furthermore, current treatment options, including pharmacological and surgical interventions, may alleviate symptoms but do not provide a permanent cure.[11] Drug therapy is symptomatic, while surgery is associated with high recurrence rates.[12] In addition, in the case of ovarian endometriomas, there is concern about the risk of damage to the ovarian reserve.[13]

In light of the limited therapeutic approaches currently available, research has been directed towards the potential of nanotechnology. Engineered delivery systems based on gold nanoparticles (AuNPs) demonstrate a high degree of versatility and potential for a wide range of applications including drug delivery and photothermal therapy (PTT).[14] PTT is a non-invasive methodology with significant potential to improve the treatment of a range of diseases. It offers numerous advantages, including reduced costs, fewer adverse effects and a wavelength suitable for biological applications. The effectiveness of the therapy has been enhanced by combining nanotechnology with PTT.[15,16] Nanomaterials have been used as photosynthetic agents,[17] capable of converting light into heat and consequently increasing the local temperature (up to 40 °C) to decrease cell viability.[17,18] In clinical practice, PTT is employed in a variety of applications, contingent upon the specific location, depth, and stage of the disease.[19] AuNPs have emerged as the most prevalent nanomaterial utilized in PTT over the past few decades.[20–23]

The use of AuNPs is largely influenced by their size and shape, which can be regulated through different fabrication techniques.[24–29]

The tunable gold properties facilitate the synthesis of nanoparticles with the desired shape and specific size, which results in a shift in plasmonic resonance from 520 to 800–1200 nm.[17] Spherical AuNPs (GNP) have received the greatest interest due to the ease with which such structures can be synthesized,[30] while nanostars, which originate from a spherical core, have recently gained much more attention due to their circular structure with protruding, pointed branches. Gold nanostars (GNS) have permitted advances in imaging and treatment due to their anisotropic architecture, which allows them to be used as contrast agents with significant signal enhancement and as photothermal agents with increased conversion of light to heat.[31,32] Despite these promising applications, they failed to progress into the clinic due to the significant accumulation in organs such as the spleen and liver, which may lead to cytotoxic effects.[33] Unfortunately, to date, several mechanisms involved in mononuclear phagocytic system (MPS) organ uptake, long-term toxicity and *in vivo* clearance are still unknown.[34]

One of the key aspects of AuNPs is the optical phenomenon produced by the oscillation of free charges on the surface of them affected by specific light incident on the gold surface, called Localized Surface Plasmon Resonance (LSPR).[16] The LSPR effect depends on the size and shape of AuNPs, thus giving the nanostructures a unique optical tuning and high photothermal conversion efficiency.[35–37] It is essential that the use of lasers with varying wavelengths be contingent upon the specific LSPR properties of the nanoparticles employed. More specifically, the use of nanostars is enhanced by the employment of an 800 nm wavelength laser, which is able to penetrate into the deepest regions of the tissue,[38–40] while nanospheres require a laser at 532 nm, a limiting factor for penetration. Indeed, the absorption coefficient of blood at 532 nm is exceedingly high, which precludes the use of lasers to irradiate deep tissue.[23,41,42] To overcome this limitation, other approaches must be exploited, such as the *in situ* irradiation through optical fiber.[43]

The objective of the presented study is to develop a novel nanosystem based on gold nanoparticles to actively target human CD44(+) endometriosis cells and significantly reduce their viability by photothermal therapy (PTT).

To this end, a biocompatible LA-PEG-Mal was employed to stabilize AuNPs of two different shapes (spheres and stars), decorated with an antiCD44 antibody (Au@P_AbCD44), whose hydrodynamic diameter was suitable for cellular uptake. In this study, the impact of Au@P_AbCD44 on interactions with three distinct cell lines was subjected to a comprehensive examination.

The cell lines included 12Z cells[44,45] with CD44 overexpression, HESC[44,46] with low CD44 expression, and NIH-3T3[47] as an internal control. The viability of cells, receptor recognition, uptake mechanisms, and internal localization of all nanoparticles were examined, respectively. The PTT effect of cell-internalized Au@P_AbCD44 was finally investigated and compared using specific laser types in all three cell lines, with an evaluation of the rate of apoptotic and necrotic cells.

2. Results and discussion

2.1. Physicochemical and biochemical characterization of Au@P and Au@P_AbCD44

Endometriosis is a chronic gynecological condition with no definitive or fully effective therapy currently available. In this work, a new therapeutic strategy was developed for endometriosis treatment using photothermal effects mediated by different laser irradiation conditions.

First, the synthesis of spherical and star-shaped nanoparticles (**GNP@P_AbCD44**, and **GNS@P_AbCD44**) was conducted in accordance with the synthetic strategy depicted in Scheme 1. This approach enabled the generation of highly stable and fully reproducible nanoparticles through the use of maleimide chemistry.[48]

Following the pegylation procedure, transmission electron microscopy (TEM) observations of the GNP@P and GNS@P complexes revealed the presence of monodispersed nanoparticles, displaying a spherical or star-shaped morphology
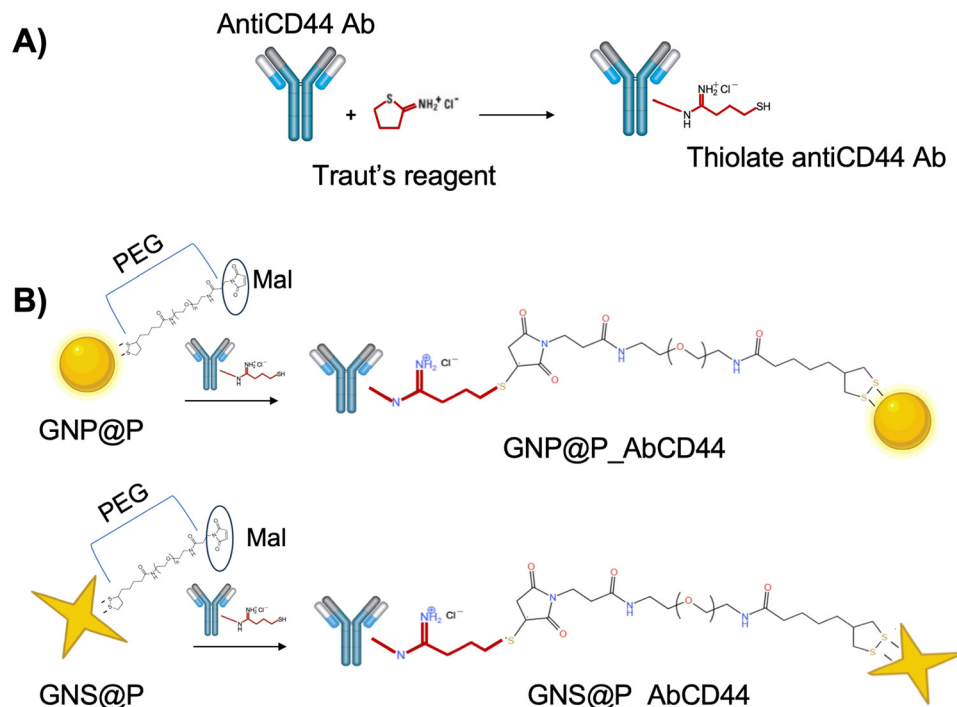
Scheme 1 Schematic representation of Au@P_AbCD44 synthesis. (A) Enrichment of the antiCD44 Ab with thiol group through Traut reagent; (B) Maleimide (Mal) Pegilated (PEG) GNP@P and GNS@P functionalized with the thiolated antiCD44 Ab to produce GNP@P_AbD44 and GNS@P_AbD44, respectively.

with a core dimension of approximately 30 nm and 35 nm, respectively (Fig. S1A and B). The pegylation process consists in the addition of PEG *i.e.* hydrophilic polymers on nanoparticles surfaces. It is crucial in protecting them from various dynamic degradation mechanisms. The presence of PEG allows the nanoparticles to remain in circulation for a longer time, avoiding cellular opsonization due to the repulsion of plasma proteins.[49–51]

As illustrated in Fig. 1A and B, the UV-vis absorption spectra of GNP@P and GNS@P exhibited a broad LSPR with a maximum at approximately 520 nm and 808 nm, respectively. This phenomenon can be attributed to the distinct spatial structures of GNPs and GNSs.[52–55]

In order to improve antibody conjugation, reactions involving a 25-fold excess of Traut's reagent, conducted for a period of 16 hours, yielded a mean concentration of 0.67 ± 0.08 mM thiol groups on the antiCD44 antibody. This resulted in the presence of 2 sulfhydryl groups per antibody. As evidenced by many authors in the literature, the use of this reagent leads to the addition of SH groups on a whole antibody and favors interaction with the maleimide groups.[56–58] The addition of the sulfhydryl groups on the antibody depends on the use of different incubation times and different amounts of Traut's reagent.[59] For the antibody conjugation, one to two thiol groups would be ideal, since it ensures an efficient reaction while preserving the immunoreactivity of the antibody.[60,61]

The proposed data were therefore in agreement with the work reported by Etienne van Bracht *et al.*,[59] where they show

that using the 25-fold excess concentration of the reagent, the ideal number of thiol groups can be obtained.

While numerous articles in the literature have employed surface modification of gold nanoparticles with hyaluronic acid (HA),[62–67] antibodies represent an intriguing platform. This choice was primarily driven by the advantages offered by antibodies, which represent a promising platform due to their ability to enhance therapeutic efficacy at the target site, minimize off-target effects, facilitate cellular internalization, and improve delivery to specific tissues.[68,69] These features contribute to increased selectivity, reduced toxicity, and improved sensitivity. Furthermore, the antibody-based approach enables more controlled and consistent surface functionalization and facilitates the quantification of receptor-mediated interactions, which is crucial for mechanistic studies.[68,69] Although HA also binds to CD44, as a natural ligand it exhibits lower binding specificity and is more prone to enzymatic degradation. These limitations could compromise both the targeting efficiency and the stability of the nanoparticle system. For these reasons, we selected the antibody-based strategy as a more robust and precise approach for our targeted delivery platform.[68,69]

Before conjugating the nanoparticles, the best AuNPs/antibody ratio was studied, considering the GNP@P and GNS@P (Fig. S3).

Three different ratios of AuNPs and antibody (1 : 1, 1 : 2 and 1 : 3) were analyzed and the results were evaluated by DLS, zeta potential, UV-vis, dot blot and BCA assay (Fig. S3). At a 1 : 1 ratio (AuNP : Ab), no significant changes in hydrodynamic size,
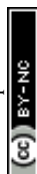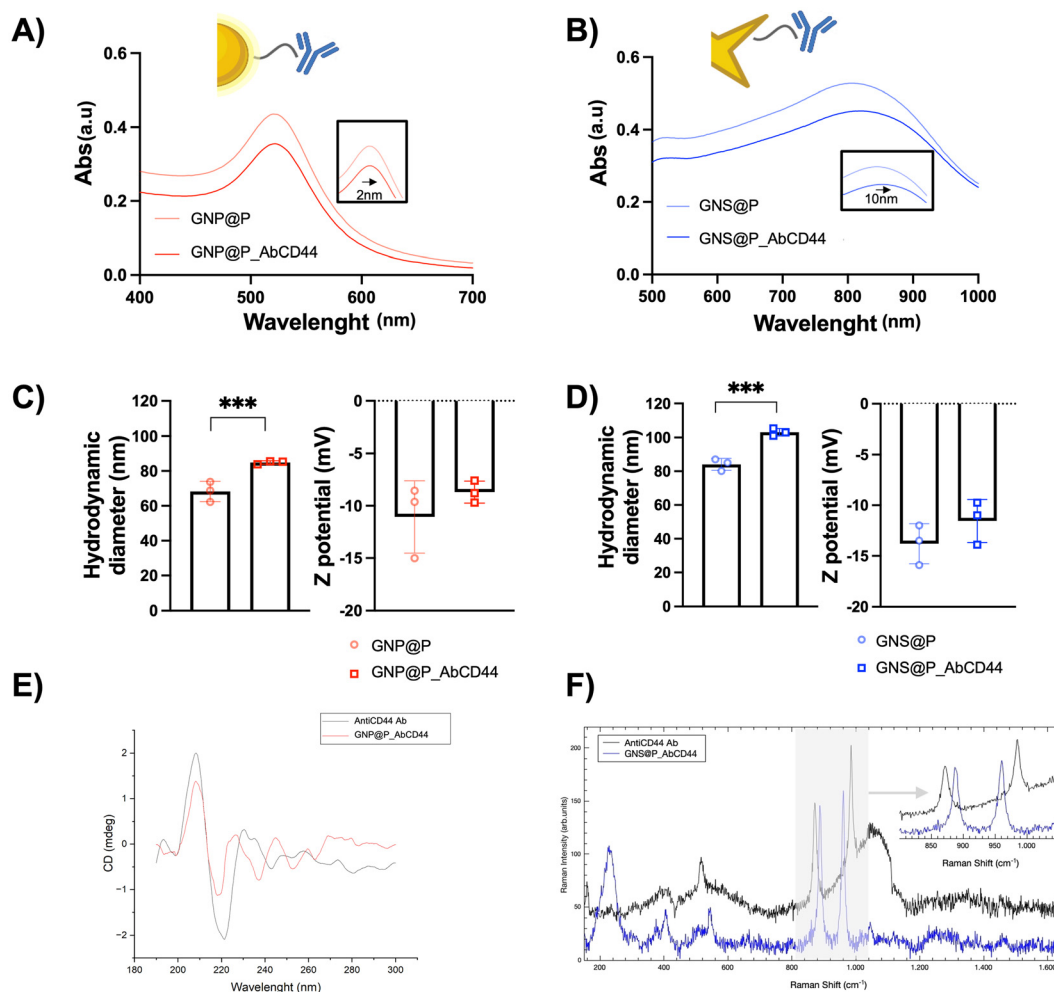
Fig. 1 Physicochemical characterization of Au@P_AbCD44. Absorbance spectrum of (A) GNP@P; GNP@P_AbCD44 and (B) GNS@P, GNS@P_AbCD44 by UV-Vis spectrophotometer. The inset indicates the peak magnification. DLS and Zeta potential of (C) GNP@P; GNP@P_AbCD44 and (D) GNS@P, GNS@P_AbCD44, respectively. (E) CD of free AbCD44 and GNP@P_AbCD44 and (F) SERS of free AbCD44 and GNS@P_AbCD44.

surface charge, or localized surface plasmon resonance (LSPR) were observed compared to Au@P. Additionally, the dot blot did not reveal the presence of antibody, and the BCA assay confirmed negligible protein binding, indicating inefficient conjugation.

In contrast, in the ratio 1:3 the conjugates exhibited a markedly increased size and surface charge, along with an exceptionally high conjugation efficiency (>85%) as measured by BCA assay with the absence of a significant redshift in the plasmonic peak. Together this data suggests that the antibodies may be densely packed and randomly oriented on the nanoparticle surface, potentially reducing the accessibility of their antigen-binding sites. This indicates that excessive surface coverage may compromise the functional orientation and targeting efficiency of the conjugates.[70,71]

An optimal balance was achieved at a 1:2 ratio, which provided moderate size increase, stable surface charge, and consistent antibody detection by both dot blot and BCA assay. This conjugation protocol was therefore selected for further

experiments and applied to both gold nanospheres (GNPs) and gold nanostars (GNS).

Following the conjugation of antibodies to the GNP@P and GNS@P, a red shift was observed in the respective bands, with wavelengths of 522 nm and 818 nm being recorded (Fig. 1A and B). The slight transition between unconjugated and conjugated nanoparticles has been previously documented in the scientific literature. For spherical nanoparticles, the shift between unconjugated and conjugated with different antibodies is normally 2–3 nm.[53,72] Whereas in the case of star-shaped nanoparticles, a greater discrepancy in the shifts between unconjugated and conjugated can be observed, probably attributable to shape differences.[54,55] To confirm the successful conjugation of the antibody onto the GNP@P and GNS@P surfaces, the size and charge of the nanosystem were evaluated using dynamic light scattering (DLS) and zeta potential techniques. In Fig. 1C and D are reported the mean hydrodynamic diameter and zeta potential for all samples. The size of the particles and the zeta potential are essential parameters

for evaluating whether the conjugated antibody is present or absent.[73] The DLS analysis revealed that the resulting GNP@P_AbCD44 and GNS@P_AbCD44 exhibited an increased hydrodynamic diameter of 16.6 nm and 19 nm, respectively, in comparison to the GNP@P and GNS@P alone (Fig. 1C and D). The findings align with the existing literature, substantiating the binding between both types of nanoparticles and the CD44 antibody.[55,72–75]

To validate the successfully conjugation, the zeta potentials (in Fig. 1C and D) indicated a slight but non-significant variation for both GNP@P and GNP@P_AbCD44, as well as for GNS@P and GNS@P_AbCD44.[72] In addition to assessing the physicochemical properties of all nanoparticle formulations tested, the effectiveness of the conjugation reaction was also evaluated. The antiCD44 antibody was conjugated to the GNP@P at an efficiency of 68.75% ± 3.78. In contrast, the conjugation efficiency to the GNS@P was found to be 58.53% ± 8.63 These results, obtained by BCA assay, indicated that the two different shape of gold nanoparticles involved in the work significantly influences their interaction with targeting molecules. To date, size and shape of the AuNPs play an important role in conjugation efficiency as previously reported.[52] The presence of the antibody was additionally verified through SDS-electrophoresis and as spots on the nitrocellulose membrane with dot blot assay (Fig. S2A and B). Furthermore, circular dichroism substantiates the presence of the antibody and additionally confirms that the antibody structure remained intact following binding (Fig. 1E), with α-helices displaying prominent positive bands in the range of 191–193 nm and negative peaks around 208–222 nm, while β-sheets show a strong positive band between 195–200 nm and a broad negative trough at 216–218 nm.[76] It was not feasible to corroborate this finding with GNS@P_AbCD44, given that the star-shaped configuration of GNS@P hinders the interpretation of the data by the instrument (data not shown). In fact, one of the challenges in characterizing GNS regards their asymmetry and irregular shape.[77,78]

To further investigate the binding between the antibody and GNS@P, surface-enhanced Raman scattering (SERS) was exploited (Fig. 1F). The huge enhancement of the Raman scattered light occurs upon the excitation of the localized surface plasmon resonances (LSPR), which are typically generated in noble metals nanostructures. Gold nanostars are among the most efficient plasmonic materials for SERS applications, enabling even single-particle detection.[79,80] To gain insight on the interaction involving the antibody and the gold nanostars, Raman and SERS measurements were performed on the solid Ab extracted, and the solid GNS@P_AbCD44. It is well known that Raman responses of antibodies are highly heterogeneous due to different interfering signals with overlapping peaks, leading to a not trivial interpretation of the data.[81] Fig. 1F shows the most recurrent Raman spectrum of Ab, which is dominated by two intense Raman bands at 871 and 986 cm^{-1}, the latter with a broadened shoulder at the higher energies. In this energy region some Raman modes from the secondary structure of the antibody and the hydrogen bonding state of

tyrosine have been observed.[81,82] Other weaker features are observed, particularly between 500–550 cm^{-1}, attributed to disulfide conformations and in the region above 1400 cm^{-1}, i.e., the amide I region.

The Raman heterogeneity typical of antibodies is further enhanced by intrinsic fluctuations due to the SERS effect.[83] But it has been possible to isolate the SERS spectrum from GNS@P_AbCD44 with similar Raman signature with respect to those observed in AbCD44. The spectrum is reported in Fig. 1F, in the inset the region where the most intense Raman modes fall is enlarged. It is very important to focus on the peak energies in this region; Indeed, the observed modes at 871 and 986 cm^{-1} in the Ab sample, in the GNS@P_AbCD44 are now centered at 886 and 960 cm^{-1}, respectively. This clearly indicates that the vibrations responsible for these signals are strongly perturbed by the enhanced electromagnetic fields acting during the SERS effect. This is in turn evidence of the interaction between antibodies and gold nanostructures.

Ultimately, both GNP@P_AbCD44 and GNS@P_AbCD44 exhibited stability in bidistilled H$_2$O for up to 28 days (analysis performed every 7 days) at 4 °C (Fig. S3), as well as in complete medium following measurements taken at 0 and 4 hours of incubation at 37 °C (data not shown). The results of the UV-vis analysis, DLS, and zeta potential measurements confirmed the stability of the samples, as indicated by the maintenance of a constant LSPR, hydrodynamic diameter, and charge.

2.2. *In vitro* Au@P_AbCD44 targeting and uptake evaluation in endometriotic cells

In order to conduct the experimental procedures with both shape of antibody-conjugated nanosystems, Au@P_AbCD44, it was essential to select an appropriate cell model and evaluate the CD44 expression. To assess the expression of CD44 in 12Z, HESC and NIH-3T3, confocal laser scanning microscopy (CLSM), dot blot, and flow cytometry were employed (Fig. S5). As a result, the 12Z cell line,[44,45] which is derived from human endometriotic epithelial tissue, exhibited a significantly heightened expression of CD44 compared to the HESC and NIH-3T3 cell types. HESC,[44,46] a human cell line derived from stromal endometrial tissue with myomas, expresses a low level of CD44, and NIH-3T3,[47] a murine fibroblast cell line is commonly used as a health cell model. To substantiate the hypothesis that Au@P_AbCD44 exhibits a selective effect toward the CD44 receptor, 12Z cell line was selected as the target cell model for further investigation, in addition to HESC and NIH-3T3 were included for comparative analysis. Thereafter, to assess cell viability, a dose-dependence experiment was conducted, in which Au@P (Fig. S5A) or Au@P_AbCD44 (Fig. 2A and B) were added to each cell type and incubated for 24 h and 72 h, respectively. The 24 µg mL^{-1} (both for Au@P and Au@P_AbCD44) concentration was identified as the highest concentration that was biocompatible for use in the subsequent experiment. In detail, the dose-dependence data of Au@P_AbCD44 indicate a slight reduction in viability in the
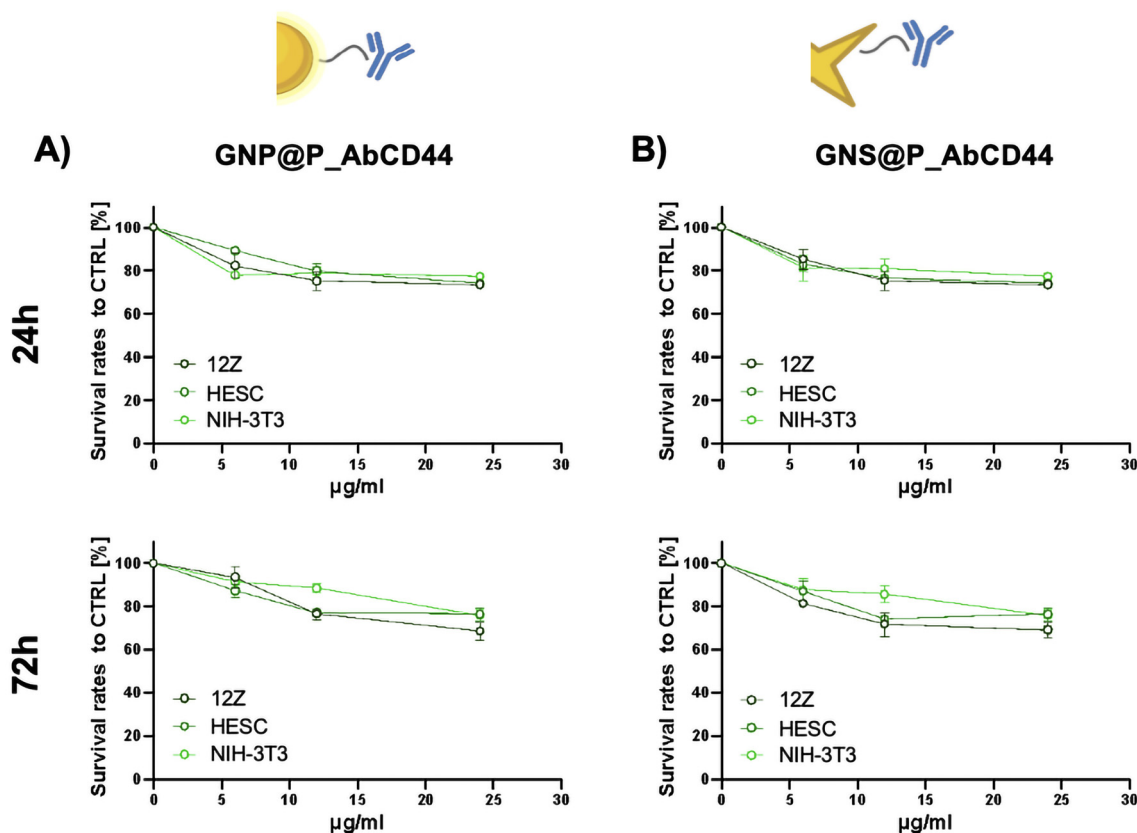
Fig. 2 Dose-dependent effects of Au@P_AbCD44 on cells viability. 12Z, HESC and NIH-3T3 cells were incubated with different concentrations of (A) GNP@P_AbCD44 and (B) GNS@P_AbCD44 ($0-24$ μg mL^{-1}) respectively. Cell viability was performed at two time points: 24 h and 72 h, respectively. Test groups were compared to untreated cells (CTRL). Data are represented as mean $\pm$ standard deviation. *$p < 0.05$; **$p < 0.01$, ***$p < 0.001$ ($n = 3$).

12Z cells when compared to the other two cell types (Fig. 2). In alignment with these findings, Kumar *et al.*[84] demonstrated that the viability of cells decreased in proportion to the quantity of gold. Specifically, 25 μg mL^{-1} of gold nanoparticles demonstrated the capacity to reduce the viability of ovarian cells by approximately 20% following a 24-hour incubation period. Additionally, Chueh *et al.*,[85] demonstrated that the reduction of viability is significantly influenced by the gold content[86,87]

The green fluorescent signals obtained by CLSM were observed exclusively in the 12Z cells, in contrast to the HESC and NIH-3T3 cells. Subsequent assessments were conducted using flow cytometry (Fig. 3A and B). The free antibody demonstrated a higher capacity for recognizing the CD44 cellular receptor compared to the gold nanoparticle conjugated antibody. Additionally, the images obtained by flow cytometry indicated that the differently shaped Au@P_AbCD44 exhibited a "spot"-like recognition pattern, unlike the antibody alone, which displayed a circular pattern. No differences in recognition between the two shapes were found.

This discrepancy is likely attributed to the reduced binding efficiency of the gold nanoparticle conjugated antibody. It may be that the antibody conjugated to the nanoparticles induces a greater affinity of the receptors at the membrane level and thus promotes an earlier internalization of the conjugated antibody.[88,89]

In addition to the effective conjugation of antibodies to gold nanoparticles and cell receptor recognition, ensuring the efficient uptake of nanovectors by cells[90] is of critical importance for the optimal therapeutic outcomes of the platform for PTT.[88,91] In the proposed study, the direct interaction between Au@P_AbCD44 and the CD44 receptor overexpressed by endometriotic cells was compared to unconjugated Au@P (Fig. 4 and S6). To illustrate the internalization of the CD44 receptor-mediated nanocarrier in pathological cells, 12Z, HESC, and NIH-3T3 cells were treated with unconjugated GNP@P and GNS@P (Fig. S6B and C), and with antibodies conjugated with both types of gold nanoparticles, GNP@P_AbCD44, and GNS@P_AbCD44, for 24 h at 37 °C (Fig. 4). The 24 h timepoint was selected based on dose-dependent viability data, which indicated lower toxicity compared to 72 h. The rapid internalization of nanoparticles in 12Z after 24 h cells was selectively achieved with both GNP@P_AbCD44 and GNS@P_AbCD44 (12 μg mL^{-1}), as evidenced by the presence of a yellow scattering signal obtained by CLSM (Fig. 4A).
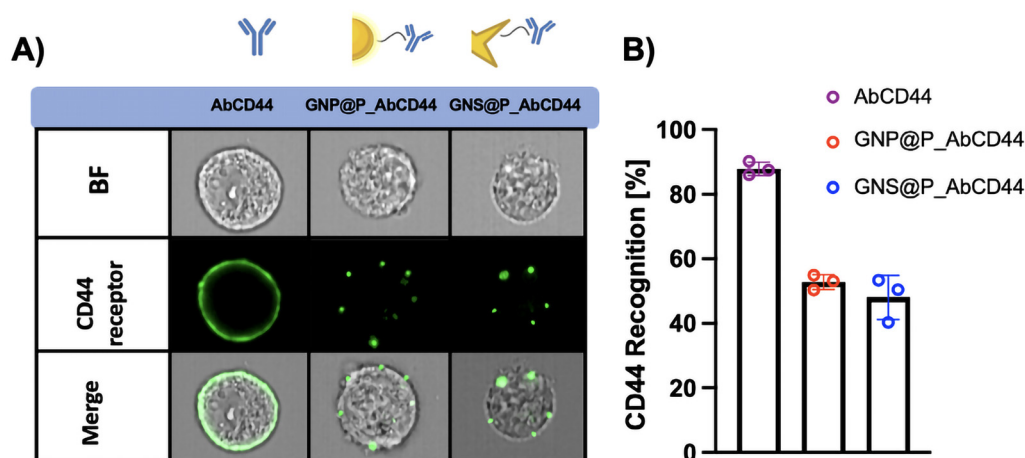
Fig. 3 Receptor recognition of Au@P_AbCD44 in endometriotic cell lines. (A) Images obtained *via* flow cytometry of 12Z cells incubated for 24 h in presence of free AbCD44 and Au@P_AbCD44, respectively. Brightfield (BF): cells; green: receptor. (B) Quantification of recognition *via* flow cytometry.
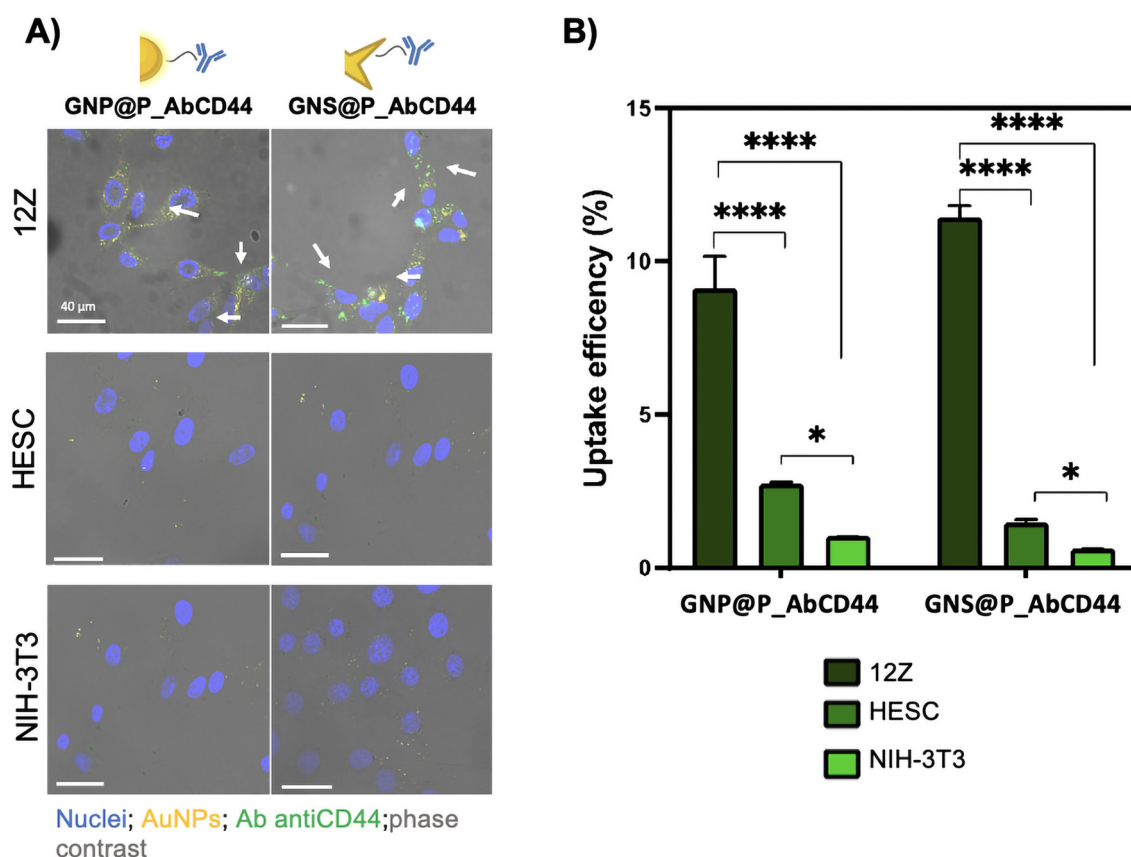

Fig. 4 Qualitative and quantitative evaluation of Au@P_CD44 internalization of 12Z, HESC and NIH-3T3 cells. (A) Images obtained by CLSM of 12Z, HESC and NIH-3T3 incubated for 24 h in presence of Au@P_AbCD44. The images were visualized in reflection bands after the excitation at 545 nm and stained in yellow (false colour); Nuclei in blue; phase contrast in grey; white arrows indicated the internalized Au@P_AbCD44. (B) Uptake efficiency obtained by ICP-MS of 12Z, HESC and NIH-3T3 incubated for 24 h with Au@P_AbCD44 (12 μg mL^{-1}). The percentage is calculated as described in materials and methods section. Data are represented as mean $\pm$ standard deviation. *$p < 0.05$; **$p < 0.01$; ***$p < 0.001$, ****$p < 0.0001$. Scale bar: 40 μm ($n = 3$).

By comparison, GNP@P_AbCD44 and GNS@P_AbCD44 were not internalized by the other two cell types within 24 hours of incubation. These findings suggest that the presence of a CD44-specific antibody on the surface of both GNP@P and GNS@P is a prerequisite for cellular internalization.[92] To corroborate these findings, a quantitative analysis by ICP-MS was conducted, demonstrating that the uptake and efficiency were significantly higher in 12Z cells (around 12%) (Fig. 4B) compared to less than 5% in HESC and NIH-3T3 cells. The same analyses were conducted with both unconjugated GNP@P and GNS@P (12 µg mL^{-1}) (Fig. S6B and C), demonstrating minimal internalization by CLSM (yellow signal) (Fig. S6B) and an uptake efficiency of less than 1% by ICP MS (Fig. S6C). Following the confirmation that both shaped types of Au@P_AbCD44 were solely internalized by the 12Z cell line, further detailed experiments were conducted to gain greater insight into the process (Fig. 5A and B). Firstly, TEM was employed to visualize GNP@P_AbCD44 and GNS@P_AbCD44 within cellular organelles and intercellular spaces, taking into account their high electron density (Fig. 5A). In TEM images, GNP@P_AbCD44 was observed as small dots, while GNS@P_AbCD44 was seen as small stars with four peaks. In higher magnification images, the localization of GNP@P_AbCD44 and GNS@P_AbCD44 within 12Z cells could be visualized with clarity. Both GNP@P_AbCD44 and GNS@P_AbCD44 were observed to localize within vesicles, in line with the results proposed by several groups.[93-95] (Fig. 5A). Furthermore, the impact of a double concentration (24 µg mL^{-1}) of both GNP@P_AbCD44 and GNS@P_AbCD44 on cell internalization was also assessed (Fig. 5B). The results indicated that a double concentration of conjugated gold

nanoparticles could facilitate internalization, suggesting that this concentration may be biocompatible and enhance uptake efficiency.

To elucidate the endocytic pathway responsible for the internalization of both GNP@P_AbCD44 and GNS@P_AbCD44 by target cells 12Z, three different endocytic pathway inhibitors were tested (Fig. 6A and B). Amiloride was selected as a macropinocytosis inhibitor,[96] while chlorpromazine was utilized as a clathrin-mediated endocytosis inhibitor (receptor-dependent mechanism).[97] Indomethacin was employed as an inhibitor of caveolae-mediated endocytosis.[98] The efficacy of the inhibitors was evaluated on an individual basis. The concurrent incubation of cells with each type of differently shaped Au@P_AbCD44 and chlorpromazine resulted in a significant inhibition of gold nanosystem uptake in 12Z cells, with an 80% reduction compared to control cells (cells treated with GNP@P_AbCD44 or GNS@P_AbCD44 but not with the inhibitors). In contrast, the concomitant administration of amiloride and indomethacin resulted in a 35% reduction in the uptake of both types of GNP@P_AbCD44 and GNS@P_AbCD44, as illustrated in Fig. 6A. CLSM images (Fig. 6B) corroborated these findings, exhibiting a pronounced scattering distribution in amiloride and indomethacin samples that differed from the ones treated with chlorpromazine. In the absence of data regarding endometriosis, a previous study observed that nanovectors capable of binding to CD44 underwent endocytosis in CD44-overexpressing cells, largely through a receptor-facilitated mechanism.[99]

Our findings supported those of previous studies, indicating that the delivery of monoclonal antibodies *via* AuNPs to their corresponding cell membrane receptors is an efficacy-enhancing approach.
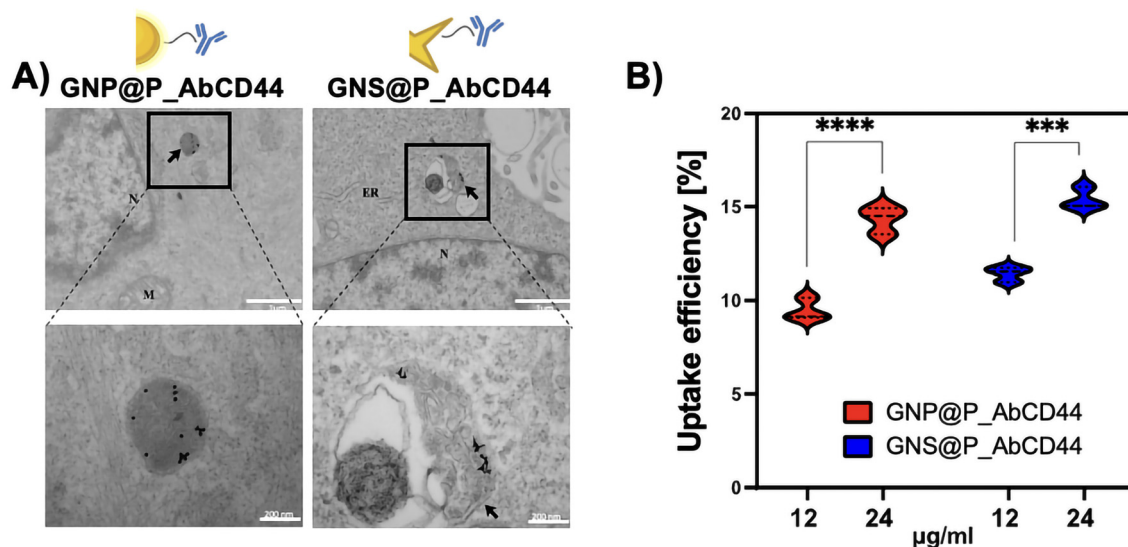

Fig. 5 Internalization of Au@P_CD44 in endometriotic target cell lines 12Z. (A) TEM images of 12Z cell incubated for 24 h with GNP@P_AbCD44 and GNS@P_AbCD44, each respectively at 24 µg mL^{-1}. (N: Nucleus; M: Mitochondria; ER: Endoplasmic reticulum; Black arrows: Vesicles containing the AuNPs). Scale bars: 1 µm, 1 µm, 200 nm, 200 nm. (B) ICP-MS data of Au@P_AbCD44 cells internalization with two different concentrations (12 µg mL^{-1} and 24 µg mL^{-1}). The percentage is calculated as described in materials and methods section. Data are represented as mean ± standard deviation. *$p < 0.05$; **$p < 0.01$; ***$p < 0.001$; ****$p < 0.0001$ ($n = 3$).
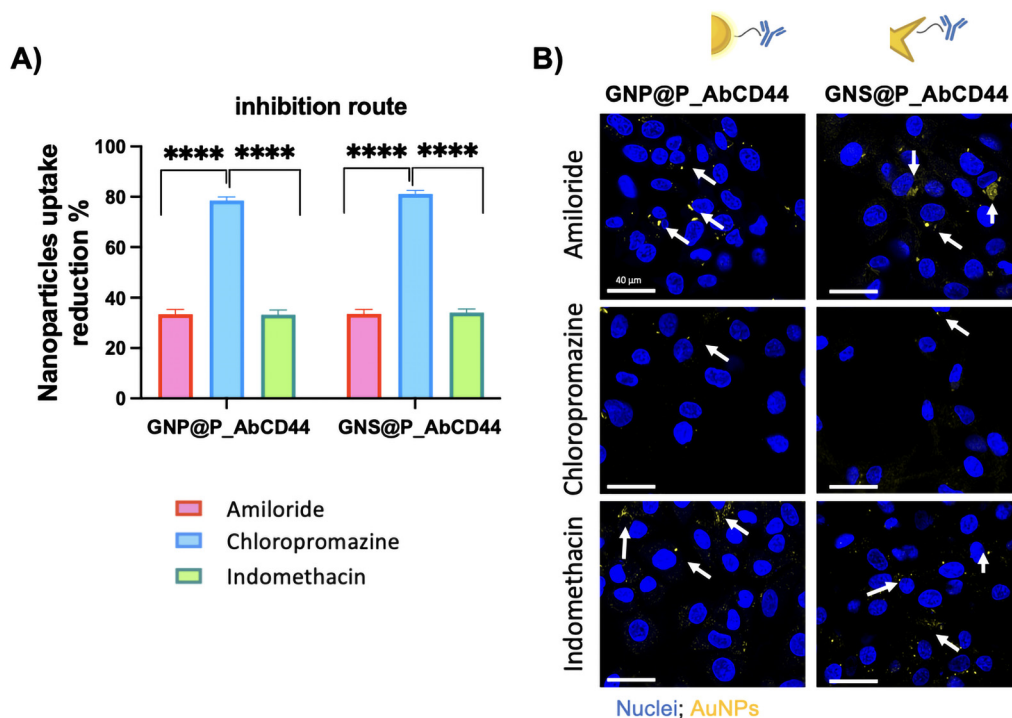
Fig. 6 Cellular uptake mechanism of Au@P_AbCD44 by 12Z cells. The uptake mechanism is quantified with (A) ICP-MS and observed by (B) CLSM. In both experiments, uptakes of Au@P_AbCD44 were analysed in presence of specific endocytosis inhibitors as described in materials and methods section. (A) ICP-MS data are expressed as nanoparticles reduction (%). (B) Scattering of Au in yellow (false color); nuclei in blue; white arrows indicated the internalized Au@P_AbCD44. Data are represented as mean $\pm$ standard deviation. *$p < 0.05$; **$p < 0.01$, ***$p < 0.001$, ****$p < 0.0001$. Scale bar: 40 μm ($n = 3$).

2.3. PTT effects on the viability of endometriotic cell-internalized Au@P_AbCD44 nanoparticles

PTT represents a non-invasive methodology with significant potential for enhancing recovery times and improving the treatment of a range of diseases, particularly cancer. It offers numerous advantages, including reduced costs, fewer adverse effects, and a wavelength well-suited to biological applications. The efficacy of the therapy was enhanced by combining nanotechnology with PTT. The nanoparticles were utilized as photosynthetic agents, capable of converting light into heat and consequently increasing the local temperature.[17,18,100,101] Despite its promising applications, the current literature contains a limited number of studies investigating the use of PTT in endometriosis.[101–103]

In this study for the first time, sphere- and star-shaped gold nanoparticles were employed as photothermal coupling agents in endometriosis due to their photothermal conversion efficiency under different laser irradiation conditions.

The initial test conducted on 300 μl of solution was to quantify the rising temperature of a complete medium dispersion of GNP@P and GNS@P under 532 nm and 808 nm laser irradiation, respectively. The two wavelengths align with the nanoparticles' LSPR (Fig. S1C and D). In particular, for GNP@P exposed to a 532 nm laser, it was necessary to utilize a complete medium devoid of phenol red, as the medium with

phenol red alone resulted in a notable elevation in temperature, due to its absorption peak around 500 nm (Data not shown). The temperature increase was found to be dependent on both the concentration of Au@P nanoparticles and the duration of exposure, reaching a plateau after 15 minutes for both laser wavelengths.

The objective of this study was to investigate the photothermal therapeutic effect of cell-internalized GNP@P_AbCD44 or GNS@P_AbCD44 by evaluating the viability of the 12Z, HESC, and NIH-3T3 cell lines following a laser treatment assay, as detailed in Fig. 7 and S8. Following the internalization of CD44-conjugated gold nanoparticles by each cell type, a specific laser irradiation[23,104] was performed at the appropriate power density (as detailed in the Materials and methods section) to achieve a maximal reduction in target cells (12Z), while avoiding interference with control cells (HESC and NIH-3T3). The laser set-ups were constructed in such a way as to maintain the environment around the multiwell plate at a constant temperature of 35 °C–37 °C. This allowed for the *in vitro* experiment to be carried out in a manner that simulated an *in vivo* situation. In general, 12Z cells demonstrated a significant decline in cell viability following irradiation with both laser types (Fig. 7B and F). Notably, a lower power is required to reduce 12Z cell viability using an 808 nm laser (Fig. 7E) compared to a 532 nm laser (Fig. 7A). Given the dimensions and configuration of the nanoparticles employed
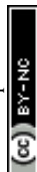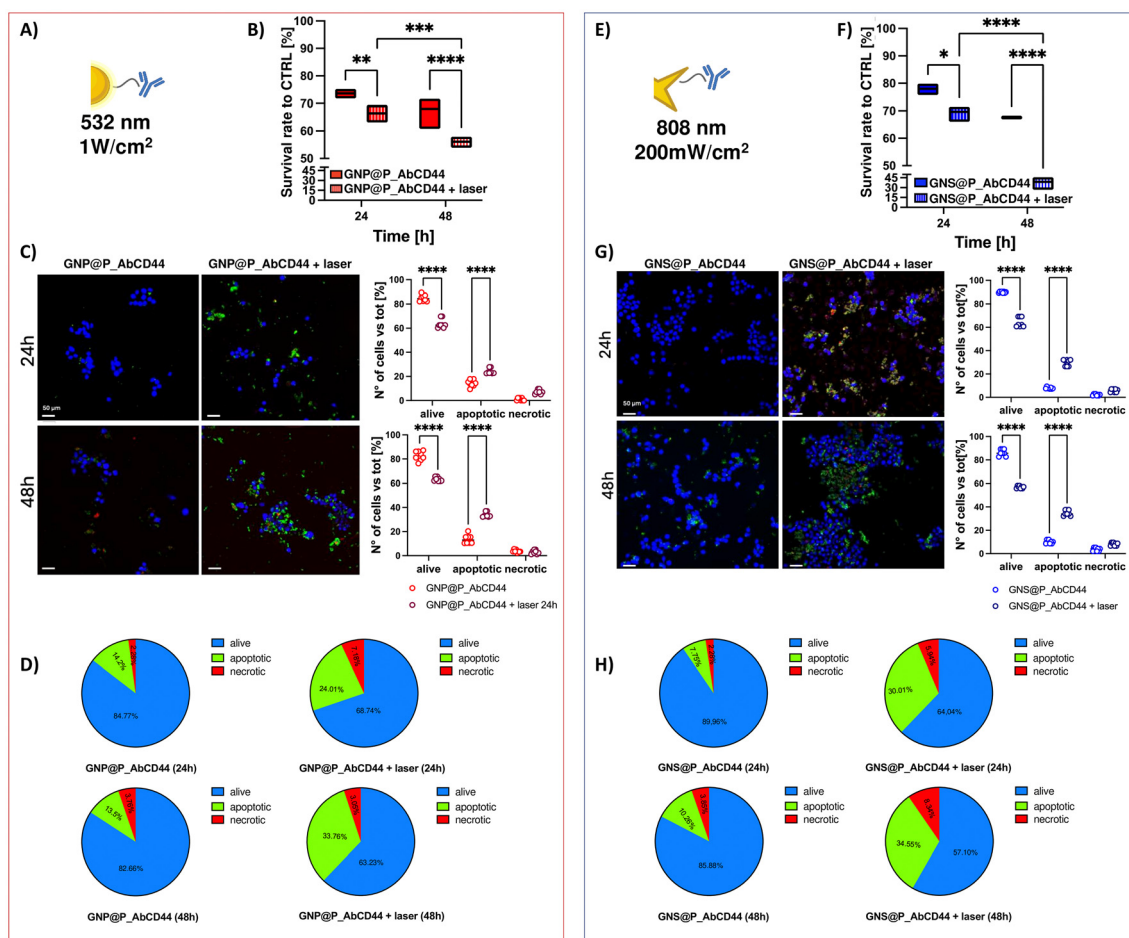
Fig. 7 PTT effect on the viability of Au@P_CD44 internalized endometriotic cells. Alamar blue assay of 12Z cells incubated with (A, B) GNP@P_AbCD44 and (E, F) GNS@P_AbCD44 and exposed to a 532 nm laser 1 W cm^{-2} and a laser 808 nm 200 mW cm^{-2}, respectively. Necrosis/apoptosis CLSM images of 12Z cells treated with (C) GNP@P_AbCD44 and (G) GNS@P_AbCD44 and exposed to a 532 nm laser 1 W cm^{-2} and a laser 808 nm 200 mW cm^{-2} (blue: alive; green apoptotic; red necrotic cells). (C and G) Representative quantitative data of the alive, apoptotic and necrotic cells in the above images. (D and H) Pie chart representing the percentage of live, apoptotic and necrotic cells treated with (D) GNP@P_AbCD44 and (H) GNS@P_AbCD44 and exposed to a 532 nm laser 1 W cm^{-2} and a laser 808 nm 200 mW cm^{-2}. Test groups were compared to untreated cells (CTRL). Data are represented as mean $\pm$ standard deviation. *$p < 0.05$; **$p < 0.01$, ***$p < 0.001$, ****$p < 0.0001$. Scale bar: 50 μm ($n = 3$).

in this study, a significant reduction of approximately 50% can be achieved by irradiating GNP@P_AbCD44 using a 532nm laser with a power density of 1 W cm^{-2}. In contrast, 200 mW cm^{-2} using an 808 nm laser is sufficient to attain a comparable outcome. This result may be explained by considering that, when the same nanoparticle concentration (expressed as μg mL^{-1}) is used, GNSs light absorption is larger than that of GNPs, and as a consequence they produce a stronger heating upon irradiation (Fig. S1). In particular, the results highlight the need for two different powers, depending on the shapes of the AuNPs, in order to achieve a temperature increase to approximately 42–44 °C.

These results collectively indicate that GNP@P_AbCD44 and GNS@P_AbCD44 play a significant role in mediated photothermal therapy, inducing toxicity to endometriotic cells while sparing healthy cells (Fig. 7B and F). Moreover, the viability of the cells was evaluated at 24- and 48-hours post-laser exposure to gain insight into their behavior. The data indicate

that cell death resulting from laser irradiation occurs over time, indicating a long-lasting effect (Fig. 7B and F). Following the demonstration that 12Z cells treated separately with each type of differently shaped Au@P_AbCD44 exhibited reduced viability in response to both specific laser treatments, the cell death pathway was evaluated using a necrosis and apoptosis kit (Fig. 7C, D, G and H).The observation of 12Z cells incubated with Au@P_AbCD44 but not exposed to laser treatment revealed that approximately 80% of the cells were viable (in blue) for both types of differently shaped nanoparticles at the two designated time points. By incubating 12Z cells with GNP@P_AbCD44 and GNS@P_AbCD44 and subsequent exposure to the respective lasers, it was observed that approximately 30% of the cell population exhibited apoptotic characteristics (visualized in green), while necrotic cells (visualized in red) accounted for around 7–10% (Fig. 7C, D, G and H). These findings suggest that cells demonstrate a heightened propensity for undergoing death through apoptosis. The data indicate

that the apoptosis rate increases 48 hours after exposure, which is consistent with the quantitative data presented in Fig. 7C, D, G and H. As illustrated in Fig. S9, 12Z cells that were not treated with Au@P_AbCD44 and did not undergo laser irradiation (untreated) did not exhibit any indications of cell death. Similarly, 12Z cells that were treated with Au@P_AbCD44 but not exposed to laser irradiation (laser treated) did not demonstrate any evidence of cell death.

In conclusion, the internalization of each type of shaped Au@P_AbCD44 nanoparticles by cells, followed by specific laser treatment, resulted in a notable increase in the percentage of apoptotic cells, as well as a concomitant rise in the proportion of dead cells, when compared to the incidence of necrosis. To date, laser irradiation energy can be modified to achieve this goal.[91] More specifically, using high-energy irradiation will result in rapid heating of the nanoparticles with consequent activation of the cell necrosis pathway. Although this strategy is effective for the ablation of established tumors, it can also induce undesirable effects such as loss of plasma membrane integrity and subsequent release of intracellular elements into the extracellular milieu.[105] In contrast, low-energy PTT triggers cell apoptosis, which can lead to beneficial immunogenic responses.[106,107] During the process of apoptosis, the cell membrane remains intact and signals, such as phosphatidylserine (PS), are transported into the extracellular portion of the membrane, marking the cell for phagocytosis. Upon encountering phagocytes, the apoptotic cells undergo a transformation that inhibits the inflammatory response.[105]

This proposed in vitro study demonstrated the potential of a PTT application utilizing cell-internalized Au@P_CD44 in a two-dimensional (2D) endometriosis model. Although GNPs are easy to obtain and bioconjugate, they have a limitation in photothermal therapy. They do not have LSPR in the NIR region, but an absorption peak around 500–600 nm.[16] To date, it can still be used for other applications such as cellular imaging,[108,109] biomarker evaluation,[110–115] drug release[116] or cutaneous application.[23,41] On the other hand, as widely demonstrated in the literature,[117,118] GNSs respond to NIR light and thus can be explored for therapies of deep lesions such as in endometriosis. The findings of the study indicated that GNS@P_AbCD44 was more effective than GNP@P_AbCD44 in reducing the viability of endometriosis cells, as by using lower laser power a similar reduction in viability can be achieved. The clinical translation of photothermal therapies depends critically on the penetration depth and efficacy of the applied laser wavelength, especially for deep-seated lesions. While the proposed study focused on cell-based experiments to establish proof-of-concept and characterize the nanoparticle platform, it is important to acknowledge the importance of in-depth tissue penetration studies. It is interesting to highlight that the use of NIR lasers (in the so called "therapeutic window" 650–950 nm), instead of visible beam, allows for reduced absorption and scattering by biological tissues. Additionally, an optical fiber device, based on biocompatible materials, for the treatment of deep tissues is under study. Future work will include in vivo experiments to evaluate the penetration of 808 nm laser light and assess therapeutic efficacy in more clinically relevant settings. These additional studies will be essential to validate the translational potential of our platform.

3. Conclusions

Endometriosis is a disease with an incidence of between 6% and 10% whose etiology remains unclear.[3] As evidenced, a multitude of molecular pathways are implicated in the pathogenesis of endometriosis,[5] such as the overexpression of CD44 in menstrual endometrial cells.[6,7,119,120] In light of the lack of curative therapies for endometriotic lesions, there is a growing belief in the potential of nanotechnology to enhance treatment outcomes. For this reason, the proposed study identifies a new therapeutic strategy for endometriosis treatment exploiting the potential of gold nanoparticles as an efficacious approach for selective and targeted phototherapy in endometriosis. Presently, a considerable number of initiatives have been undertaken with the objective of obtaining gold nanoparticles by means of green and safe methodologies.

In this study, two different shapes of gold nanoparticles, gold nanospheres and gold nanostars, were synthesized and conjugated to antiCD44, employing LA-PEG-Mal as a stabilizing agent. The resulting nanovectors were evaluated in vitro for their potential use in endometriosis photothermal therapy.

The synthesis methodology employed an innovative protocol, offering notable advantages in comparison to existing approaches. Primarily, the exploitation of the maleimide chemistry ensured the long-term stability of the hybrid nanomaterial, which exhibited no cytotoxicity. This was achieved through the utilization of Au–S soft–soft interactions.[121,122] Furthermore, the use of an instant reducing reagent ($NaBH_4$) ensured the production of homogeneously sized and tailored "on demand" gold nanoparticles by precisely adjusting the concentration of cCl_4. The proposed protocol yielded a nanovector that was characterized using physical and biochemical techniques. The conjugation efficiency was found to be 68.75% ± 3.78 for GNP@P_AbCD44 and 58.53% ± 8.63 for GNS@P_AbCD44, respectively. Additionally, the nanovector demonstrated stability for up to 28 days at 4 °C.

The viability and cellular uptake behaviors were investigated in two non-endometriotic cell lines, HESC and NIH-3T3, and in one endometriotic cell line, 12Z. The results showed that both Au@P_AbCD44 were biocompatible at a concentration of 24 μg mL^{-1} for all three cell lines. Furthermore, it was demonstrated that Au@P_AbCD44 (GNP@P_AbCD44 and GNS@P_AbCD44) exhibited markedly enhanced cellular internalization in 12Z cells, irrespective of nanoparticle morphology, following the activation of the classical clathrin-mediated endocytosis. This finding was also confirmed by TEM images, which revealed the presence of both types of Au@P_AbCD44 within intracellular vesicles.

Here, for the first time, sphere and star-shaped gold nanoparticles were used as photothermal agents for endometriosis

treatment.[101,102] The PTT effect was assessed on Au@P_AbCD44 internalized by the 12Z cell line, which is a model of endometriotic cells. The results of the proposed investigation demonstrated that variations in the shapes of AuNPs exert a considerable influence on their PTT effects.[17,23] Although both nanoconjugates demonstrated substantial PTT efficacy in impairing the viability of 12Z cells, solely the GNS@P_AbCD44 nanoconjugate enabled a reduced energy output to be delivered to the cells in comparison to GNP@P_AbCD44. Due to their LSPR characteristic, GNPs exhibit a lower heating efficiency than GNS under PTT.[18,123] In fact, two different lasers powers were required to reach a temperature of 42–44 °C depending on the shape of the AuNPs. In contrast to GNS@P_AbCD44, GNP@P_AbCD44 may not be considered as the optimal candidates for PTT due to their limited absorption in the near infrared (NIR) region, which is an important requisite for this application.[23,41,42] GNP@P may have the potential to be utilized for the development of nanosystems for the purpose of endometriosis imaging.[113–115] The development/validation of laser devices such as fiber optic coupled with lasers will facilitate the application of these light-responsive nanomaterials in deep-seated areas.

In conclusion, the reported results show the way for the optimization and employment of our findings in future studies for diagnostic and/or therapeutic purposes in the clinical management of endometriosis. The nanovector can be administered with existing pharmacological treatments without compromising their efficacy or safety. Although current drugs are ineffective, combining them with this treatment could overcome these limitations and improve overall therapeutic efficacy. Further studies are therefore needed to validate them in clinical use, however studies on 3D models and *in vivo* testing could implement knowledge and confirm the efficacy of the proposed nanosystem. It is our firm conviction that there is considerable potential for the development of synergistic phototherapy nanovectors as novel and efficacious endometriosis therapeutics platforms.

4. Materials and methods

4.1. Synthesis and pegylation of gold nanoparticles (AuNPs)

AuNPs, sphere and star-shaped, were synthesized by the Turkevich method as previously described.[124–126] Briefly, gold nanospheres (GNPs) were prepared using the citrate reduction method by adding tetrachloroauric acid trihydrate ($HAuCl_4$) solution to bidistilled H_2O under magnetic stirring. After boiling, trisodium citrate dihydrate was added. Magnetic stirring was continued under ambient conditions for 2.5 hours at room temperature (RT). Gold nanostars (GNSs) were prepared from the GNPs using the seed growth method, which involves the use of lauryl sulfobetaine (LSB) and GNPs as seed.[127] Briefly, seed solution was prepared first by addition of $HAuCl_4$ solution to LSB solution. Then, ice cooled sodium borohydride ($NaBH_4$) solution was added. The mixture was gently hand shaked and kept in an ice bath. Simultaneously, the growth

solution was prepared by mixing LSB solution, silver nitrate (AgNO3), $HAuCl_4$ solution and ascorbic acid (AA) solution. The seed solution was added to the growth solution and gently hand shaked for a few seconds. Finally, the seed solution was added, during which the suspension could be observed turning from pink to purple, blue and grey-blue colloid suspension. At this point, the mixing was stopped. The GNSs and GNPs were stabilized by grafting a thiolated polyethylene glycol (HS-PEG) of a high molecular weight on their surface. In particular, it was employed a lipoic acid-Poly (ethylene glycol)-Maleimide (LA-PEG-Mal) (MW 5000) (Biopharma PEG, USA), with a thiol at one end and a maleimide structure on the other end of the chain. The pegylation process involved the addition of the thiol PEG (0.1 mg mL^{-1}) overnight. Synthesis impurities and excess of LA-PEG-Mal after coating were removed with three cycles of ultracentrifugation for 40 min at 10 000g. After the third centrifugation phase, the pellets were resuspended in bidistilled H_2O, centrifuged again, and then finally resuspended in 100 mL bidistilled H_2O and stored at 2–8 °C. The actual Au molar concentration of both colloidal solutions was measured by oxidizing a small volume with aqua regia and with inductively coupled plasma optical emission spectroscopy (ICP-OES) (OPTIMA 3000 PerkinElmer instrument, Italy). Transmission electron microscopy (TEM) analysis was performed by using a TEM JEM 1200 EX II (JEOL, Peabody, MA, USA) electron microscope operating at 100 kV. Briefly, 10 μL of gold GNP@P, GNS@P in bidistilled H_2O (20 μg mL^{-1}) was deposed on Parlodion membranes (Fig. S1A and B).

4.2. Antibody conjugation to Au@P

In order to conjugate antibodies to the two different shaped GNP@P and GNS@P, a sulfhydryl group was introduced on the antibody that can react with maleimide-modified GNP@P and GNS@P (Scheme 1). The quantification was performed immediately after modifying the antibodies to prevent dimerization by oxidative disulfide bridge formation. The conjugation of GNP@P and GNS@P was performed with murine antiCD44 monoclonal antibody that specifically targets human tissue (Abcam, UK) and were obtained allowing Maleimide chemistry coupling techniques.[128] GNP@P and GNS@P were conjugated to antiCD44 antibodies to act selectively with cells that overexpress CD44 receptors. Three different ratios of AuNPs and antibody (1:1, 1:2 and 1:3) were analyzed though DLS, zeta potential, UV-vis, dot blot and BCA assay (Fig. S3) to find out which was the best AuNPs/Ab ratio.

Briefly, 2 mg mL^{-1} of 2-Iminothiolane hydrochloride (Traut's reagent-Sigma Aldrich, USA) was dissolved in 2 mM Ethylenediaminetetraacetic acid (EDTA) phosphate buffered saline (PBS) 1× pH 8.0 and then diluted 1:10. After, the desired concentration of Traut's was added to 50 μg of antibody. The solution was brought to a final volume of 500 μl with 2mM EDTA PBS 1× pH 8.0. Then it was kept in rotation for 1 h. When the reaction of thiol group's addition is finished, the antibody was purified on Amicon Ultra centrifugal filter devices (Millipore, USA) and then concentrated. To analyze the effectiveness of the Traut's Reagent, the amount of

sulfhydryl (SH) groups added on the antibody was evaluated with 5,5′-Dithiobis(2-nitrobenzoic acid) (Ellman's reagent-Sigma Aldrich). The absorbance was measured at 412 nm with Clariostar™ microplate reader (BMG-Labtech, DE) and it was transformed into the amount of sulfhydryl (SH) groups based on the calibration curve of L-cysteine (Sigma-Aldrich).[129,130] 80 µg mL^{-1} of thiolated antibodies were immediately used for the conjugation reaction to 40 µg mL^{-1} of GNP@P and GNS@P, previously centrifuged for 40 min at 10 000g at 4 °C. Conjugation occurred for 16 h in an end-over-end at 4 °C. At the end of the incubation, the samples were centrifuged for 40 min at 10 000g at 4 °C, the supernatant that contains free antibody was applied for Bicinchoninic Acid (BCA) assay. The pellet was resuspended with bidistillated H$_2$O, and two washes were performed to completely remove the unconjugated antibody by centrifuging for 40 min at 10 000g at 4 °C. The supernatant was removed, and the pellet was resuspended with bidistillated H$_2$O for further analyses. Hence, as previously reported by Bloise et al.,[52] the theoretical number of antibodies bound to gold nanoparticle ratio (AbCD44/AuNP) could be determined for GNP@P_AbCD44. Accordingly, AbCD44/AuNP = 0.67.

4.3. Physicochemical characterization of Au@P and Au@P_AbCD44

The different shape of Au@P_AbCD44 obtained was characterized by UV-Vis spectroscopy (UV-Vis); Dynamic Light Scattering (DLS); Circular dichroism (CD); and surface-enhanced Raman scattering (SERS) (Fig. 1).

UV-Vis. UV-Vis absorption spectra were measured using HJ1908003 (Aurogene, Italy) in the wavelength range of λ ~200–1100 nm at the resolution of 1 nm, using quartz cuvettes. The analyses were carried out using 40 µg mL^{-1} in bidistillated H$_2$O suspension.

DLS. The mean hydrodynamic diameter (Z-average size), and zeta-potential of Au@P and Au@P_AbCD44 were measured using a Zetasizer Nano ZS90 Malvern instrument at 25 °C (Malvern Instruments Ltd, Malvern, UK). The nanoparticle charges were determined using the same instrument for the zeta potential measurements. The analyses were carried out as reported using 40 µg mL^{-1} nanoparticles aqueous suspensions prepared using MilliQ H$_2$O. The measurements were conducted in three different times, and the reported values represent the mean of 10 analysis.

CD. The secondary structure of the AntiCD44 Ab free (20 µg mL^{-1}) and AntiCD44-conjugated gold nanoparticles (20 µg mL^{-1}) were evaluated with CD using the same parameters adopted by Bloise et al.[52] Briefly, the instrument used was Jasco J710 spectropolarimeter (Jasco Corp., Japan) at 25 °C with a 1 cm path-length quartz cell under the following conditions: 300–190 nm spectral range, 2 nm of bandwidth, 200 nm min^{-1} of scan speed and 3 accumulations Data was processed using 10-point smoothing in Origin 6.0 (OriginLab Corporation, MA).

SERS. The binding between AntiCD44 Ab free and gold nanoparticles was evaluated through SERS. Briefly, 40 µg mL^{-1}

of AntiCD44 Ab free and AntiCD44-conjugated gold nanostars was lyophilized and placed on a glass slide. SERS measurements were carried out at room temperature (RT) by using an XploRA Plus HORIBA Scientific spectrometer, coupled with an Olympus BX43 microscope. The 638 nm laser wavelength was used to irradiate the system. The samples, mounted on a motorized xy stage, were tested with a 50× objective leading to a laser spot of about 2 µm. The resulting spectral resolution was ≈3 cm^{-1}. The spectra were collected with an integration time of 30s and a number of accumulations equal to 10. Different acquisitions were collected in different areas of each sample.

4.4. Efficiency of antiCD44 antibody conjugation

The conjugation efficiency was evaluated through direct (*Sodium Dodecyl Sulphate Polyacrylamide Gel Electrophoresis-SDS-PAGE and dot blot assay*) and indirect (*Bicinchoninic acid assay – BCA assay*) techniques (Fig. S2A and B).

SDS-PAGE. SDS-PAGE was employed to validate the conjugation of antiCD44 antibody with GNP@P and GNS@P, using as a control the AntiCD44 Ab free and GNP@P and GNS@P. The samples were initially mixed with loading buffer 1× (0.25 M Tris–HCL pH 6.8; 10% sodium dodecyl sulfate (SDS) (w/v), 0.25% bromophenol blue (w/v); 50% glycerol (v/v)) in a reducing condition using Dithiothreitol (DTT-GeneSpin, Italy) and boiled for 5 min at +100 °C. Each sample was placed on a 12% polyacrylamide. To accomplish gel separation, samples were electrophoresed using Tris–glycine–SDS running buffers. Subsequently, the protein concentrations were assessed by treating the gels in a Coomassie Brilliant Blue coloring solution (1 g L^{-1} Brilliant blue, 50% methanol; 10% acetic acid and 40% bidistillated H$_2$O) and then soaking them in a destaining solution (45% methanol and 10% glacial acetic acid (v/v)). Finally, the gels were then transferred into bidistillated H$_2$O. A 10–245 kDa protein marker (GeneSpin) was used as the molecular mass standard in the SDS-PAGE measurements.

Dot blot. The presence of antiCD44 antibody on the surface of nanoparticles was assessed by dot blot assay. In brief, 5 µl of pelleted GNP@P_AbCD44 and GNS@P_AbCD44 were spotted on nitrocellulose membrane Amersham Hybond ECL (GE Healthcare Life Sciences, US) and air-dried. Unconjugated GNP@P and GNS@P were used as controls. The non-specific sites were blocked in 5% Bovine Serum Albumin (BSA) in TBS containing 0.05% Tween 20 for 1 h at RT. The membrane was then submerged in goat anti-mouse-HRP-conjugated antibody (Dako, Italy) (1 : 1000) for 1 h at RT and after wash, the signal was developed with enhanced chemiluminescence substrate (ECL Star, Euroclone, Italy) and ImageQuant LAS4000 Imaging System (GE Healthcare Life Sciences).

BCA assay. The efficiency of conjugation to nanoparticles was determined by indirect BCA approaches. In short, both GNP@P_AbCD44 and GNS@P_AbCD44 (20 µg mL^{-1}) were centrifuged for 40 min at 10 000g at 4 °C, then the supernatants were collected to determine the unbound antiCD44 antibody concentration by BCA assay (Pierce Biotechnology Inc., USA).

The quantification of AntiCD44 antibody bound to nanoparticles was determined by subtracting the amount in the supernatant from the initial quantity. The conjugation efficiency (CE) percentage was calculated as follows:[131]

$$\% \ CE = \frac{\text{total amount of antibody added} - \text{unbound antibody}}{\text{total amount of antibody added}} \times 100.$$

4.5. Stability of Au@P_AbCD44 in bidistilled H$_2$O and culture media by UV-Vis and DLS

Prior to all biological investigations, each suspension of Au@P_AbCD44 was centrifuged, resuspended in bidistilled H$_2$O and maintained at 4 °C. Every 7 days, it was subjected to UV absorbance, DLS and zeta potential measurements up to 28 days. The pH was also monitored and demonstrated stability over the 28-day period (Fig. S4A–D). Additionally, the pelleted Au@P_AbCD44 were re-suspended in the complete cell culture medium suitable for the specific cell line and incubated at 37 °C in static condition. Size variations were monitored through dynamic light scattering (DLS) measurements at time 0 (immediately after dispersion in the media) and after 4 hours of incubation (Fig. S4E–H).

4.6. Cell lines and culture conditions

Three different cell lines were used for this study: two cell lines expressing different level of CD44 receptors: 12Z and HESC obtained from abm (Canada) and a fibroblastic cell line with low expression of CD44, NIH-3T3, obtained from ATCC (USA) and used as negative control. 12Z and HESC cells were cultured in DMEM F12 medium (Euroclone) supplemented with 10% fetal bovine serum (FBS, Euroclone), 1% of penicillin–streptomycin (Lonza, CH) and 1% of L-glutamine (Lonza). NIH-3T3 cells were cultured in DMEM high glucose (Euroclone) supplemented with 10% of bovine calf serum (BCS, Euroclone), 1% of penicillin–streptomycin (Lonza) and 1% of L-glutamine (Lonza). All these cell lines were incubated at 37 °C in a humidified chamber with 5% CO$_2$ and cultured in an exponential growth phase by subcultivation.

4.7. Qualitative and quantitative assessment of CD44 expression in cell lines

To analyze the expression of CD44, Confocal Laser Scanning Microscopy (CLSM), dot blot and flow cytometry were conducted.

Qualitative techniques. The qualitative experiments were carried out *via* CLSM (Fig. S5A).

CLSM. 12Z, HESC and NIH-3T3 cells were seeded on cover glasses with a density of 3 × 10^4 cells in a 24 well culture plate. At the end of the culture time, the cells were washed with PBS, fixed with 4% (w/v) paraformaldehyde (PFA) solution for 15 min, and blocked with 3% of BSA in 1× PBS for 1 hour at RT. Cells were treated with antiCD44 antibody free (10 µg mL^{-1}) overnight (O/N). Lastly, cells were exposed to Alexa-Fluor-488 conjugated anti-mouse secondary antibodies (diluted 1 : 1000; Bethyl, USA) for 45 minutes at RT (excitation/emission maxima ~495/519 nm). Following the incubation, cells were rinsed with PBS and Hoechst 33 342 solution (2 µg mL^{-1} in 1× PBS; excitation/emission maxima ~361/497 nm; Sigma Aldrich) were used to stain the nuclei. Finally, samples were observed with a CLSM (Leica TCS SP8 DLS, Leica Microsystems, German).

Quantitative techniques. The quantitative data were performed by dot blot and flow cytometry (Fig. S5B and C).

Dot blot. Proteins were obtained from the three cell lines by lysing the cells with 1× RIPA buffer (diluting the 10× RIPA in sterile bidistilled H$_2$O, EDM Millipore Corporation, Chemicon) with the addition of protease inhibitors and phosphatases and then quantified by BCA assay. Increasing concentrations of protein (0.5 µg mL^{-1}–1.5 µg mL^{-1}) were deposited on nitrocellulose membrane Amersham Hybond ECL (GE Healthcare Life Sciences). After blocking nonspecific sites, the membrane was incubated with murine antiCD44 antibody (2 µg mL^{-1}) (Abcam) overnight at 4 °C and the final procedure was followed as reported in section 4.4.

Flow cytometry. 12Z, HESC and NIH-3T3 cells were seeded with a density of 5 × 10^5 cells in a 12 well culture plate. After 2 days, cells were detached and centrifuge at 1200 rpm for 3 min to have the pelleted cells. All the three cell lines were incubated with free antiCD44 antibody (10 µg mL^{-1}) for 1 h, washed with PBS and incubated with Alexa-Fluor-488-conjugated secondary antibodies anti-mouse (diluted 1 : 1000) (Bethyl) for 45 min at RT. After treatments, cells were washed, and analyzed by BD FACS Lyric (Becton Dickinson, USA).

4.8. *In vitro* biological characterization of Au@P and Au@P_AbCD44

Different techniques were investigated to evaluate viability (MTT assay), Cell Receptor recognition (CLSM and Flow cytometry), and cell internalization (CLSM, ICP-MS and TEM). In this study, nanoparticle concentration is expressed in terms of gold mass (µg mL^{-1}) rather than particle number. While estimating particle numbers is relatively straightforward for spherical nanoparticles, it becomes challenging for irregularly shaped nanostars. Their complex morphology and the presence of organic surface coatings influence hydrodynamic size without proportionally affecting the gold content, leading to unreliable particle number estimations. Approximating nanostars as spheres can result in significant over- or underestimation of both their volume and concentration. Therefore, gold mass concentration was adopted as a consistent and reliable metric for comparing nanoparticle dosing across experimental conditions.[132]

MTT viability assay. All the three cell lines were seeded at 1 × 10^4 cells per well 96-well plates and cultured for 24 h. Following the removal of the culture medium, cells were incubated with media containing different concentrations (0–50 µg mL^{-1}) of each type of pegylated gold nanoparticles (GNP@P and GNS@P) for 24 h and 72 h (Fig. S5A). At the end of incubation, the quantitative 3-[4,5-dimethylthiazol-2-yl]-2,5 diphenyl tetrazolium bromide (MTT – Sigma Aldrich) assay was per-

formed to assess the metabolic condition of the cells, as outlined in prior studies.[52] Once the optimal concentration of pegylated nanoparticles had been established, cells were seeded at a density of 1×10^4 per well of a 96-well plate. Following a 24-hour culture period, the cells were treated with GNP@P_AbCD44 and GNS@P_AbCD44 (0–24 µg mL^{-1}) for 24 and 72 hours, respectively. Following the incubation periods, an MTT assay was conducted to evaluate the dehydrogenase activity (Fig. 2A and B). In both analyses, cell viability was measured and expressed as a percentage related to the CTRL (untreated cells) set equal to 100%. Subsequently, the ability of the conjugate to recognize the CD44 receptor expressed by the cells and to internalize it was evaluated.

Cell Receptor recognition. The ability of Au@P_AbCD44 to recognize the receptor overexpressed by endometriotic cells was investigated by CLSM (qualitative test) (Fig. S7) and flow cytometry (quantitative test) (Fig. 3A and B). To minimize fluorescence quenching by gold nanospheres and nanostars, which are known to quench nearby fluorophores such as Alexa Fluor 488, nanoparticles surfaces were functionalized with LA-PEG-MAL spacers.[133–135] These spacers increase the distance between the fluorophore and the gold surface, thereby reducing quenching effects. To ensure the reliability of our fluorescence measurements, we incorporated multiple internal controls (data not shown): free fluorophore without nanoparticles, nanoparticles without fluorophore, cells stained with fluorophore in the absence of nanoparticles, and cells treated with nanoparticles in the absence of fluorophore. These controls allowed us to account for background fluorescence, potential autofluorescence, and nanoparticle-induced quenching, enabling accurate interpretation of the biological fluorescence signals.

CLSM. Briefly, 12Z, HESC and NIH-3T3 were seeded with a density of 3×10^4 cells per well on cover glasses placed at the bottom of a 24-well plate. After 48 hours, the medium was removed, and the cells were treated as previously described in section 4.7. Then Au@P_AbCD44 and the antibody alone were added to the cells overnight at 4 °C. Images were acquired with a confocal fluorescence microscope (Leica TCS SP8 DLS, Leica Microsystems).

Flow cytometry. 12Z cells were seeded with a density of 5×10^5 cells in a 12 well culture plate. After 2 days, cells were treated as previously described in section 4.7. Cells were incubated with Au@P_AbCD44 and free antiCD44 antibody (10 µg mL^{-1}) for 1 h, washed with PBS and incubated as described in section 4.7. The samples were analyzed by ImageStreamX Mark II (Amnis/Luminex, USA).

Cell Internalization. The internalization capacity of Au@P_AbCD44 in the three cell lines was investigated through CLSM (Fig. 4A and S5B) and uptake studies by Inductively Coupled Plasma Mass Spectrometry (ICP-MS) (Fig. 4B and 5B). Once it was established that the highest amount of gold was detected in endometriotic cells, the localization was evaluated by transmission electron microscopy (Fig. 5A), and the endocytosis pathway was identified as occurring exclusively in 12Z (Fig. 6).

CLSM. 12Z, HESC and NIH-3T3 were seeded at a concentration of 3×10^4 cells onto cover glass placed at the bottom of a 24 well culture plate. Following a 24-hour culture period, the cells were incubated with Au@P (Fig. S5B) and Au@P_AbCD44 (Fig. 4A) for an additional 24 hours. The cells that were not treated served as the control group. At the conclusion of the culture period, the cells were treated in accordance with the previously described methodology in section 4.7. Subsequently, the cells were incubated with secondary antibodies and observed with a confocal fluorescence microscope (Leica TCS SP8 DLS, Leica Microsystems) The gold nanoparticles were observed in reflection bands at 545 nm.

ICP-MS. All types of cell lines were plated 1×10^6 cells on a 6-well plate and treated for 24 h with 12 µg mL^{-1} of Au@P (Fig. S5C) and Au@P_AbCD44 (Fig. 4B), respectively, while 12Z were treated also with Au@P_AbCD44 (24 µg mL^{-1}) (Fig. 5B). After treatment, cells were washed with PBS to remove non-internalized AuNPs, trypsinized to obtain the cellular pellet, which was then incubated with 1× RIPA buffer (prepared by diluting 10× RIPA in sterile distilled H$_2$O, EDM Millipore Corporation, Chemicon) on ice for 30 minutes. The solution was transferred to a sterile Eppendorf tube and centrifuged at 13 000 rpm for 15 minutes at 4 °C.

The supernatant was removed, and the pellet was incubated with 750 µL of freshly prepared aqua regia. The samples were diluted to 3 mL with distilled H$_2$O and analyzed for Au content using ICP-MS (ELAN DRC, PerkinElmer, Italy). The nanoparticles uptake efficiency per cell was calculated as previously described.[136]

$$\text{Uptake efficiency}\,(\%) = \frac{\text{number of NPs taken up by cells}}{\text{number of NPs incubated with cells}} \times 100$$

TEM of internalized Au@P_AbCD44 in 12Z cells. 12Z cells were seeded at a concentration of 4×10^4 cells on a 24-multiwell for 24 h at 37 °C. Cells were incubated with/without nanoparticle suspensions (24 µg mL^{-1}) for 24 h. Following trypsinization cells were centrifuged at 800 rpm for 10 minutes and then fixed with 2.5% glutaraldehyde in culture medium for 2 hours at RT. The cell pellet was then rinsed in PBS, postfixed in 1% aqueous OsO$_4$ for 2 hours at RT and rinsed in bidistillated H$_2$O. Cells were pre-embedded in 2% agarose, dehydrated using graded acetone, and then embedded in epoxy resin (Electron Microscopy Sciences, EM-bed812). Ultrathin sections (60–80 nm) were cut on a Reichert OM-U3 ultramicrotome, collected on nickel grids (300 Mesh), and then stained with uranyl acetate and lead citrate. The specimens were observed with a JEM 1200 EX II (JEOL, Peabody, MA, USA) electron microscope operating at 100 kV and equipped with a MegaView G2 CCD camera (Olympus OSIS,Tokyo, Japan).[137]

Endocytosis pathway determination. 12Z cells were seeded in 6-well culture plates (1×10^6 cells per well) and after 24 h incubated with different endocytosis inhibitors as already described.[52] Briefly, 2.5 mM amiloride (Sigma-Aldrich), 2.5 µg mL^{-1} chlorpromazine (Sigma-Aldrich) and 100 µM indo-

methacin (Sigma-Aldrich) were incubated with the cells for 1 h at 37 °C with 5% of CO_2-air. When the inhibitors were removed, the cells exposed to 24 μg mL^{-1} of GNP@P_AbCD44 and GNS@P_AbCD44 in complete medium for 24 h, respectively. ICP-MS protocol was followed as described in the previous section. The data were expressed in percentage to 12Z cells not treated with inhibitors and set as 100%. In order to qualitatively evaluate the endocytosis pathway, cells were seeded on cover glass for 24-multiwell and incubated with the inhibitors as described above. At the end of the culture time, protocol described in section 4.7 was followed. The gold nanoparticles were observed in reflection bands following excitation at 545 nm.

4.9. Photothermal therapy of GNP@P_AbCD44 and GNS@P_AbCD44

Laser system setup for PTT. For the experiment two different wavelength lasers were used. The laser beam at 532 nm (continuous wave, CW) is obtained from a frequency-doubled Nd: YVO source. On the other side, the 808 nm CW laser source is a Titanium-sapphire laser used in the free-running regime. The culture plates were irradiated from the top up, with a light intensity of 1000 mW cm^{-2} and 200 mW cm^{-2} respectively. Both the irradiation setups were thermostatically controlled, allowing us to keep the multi-well plate at 37 °C for the whole time required by the irradiation phase.

Photothermal ability of Au@P. Prior to all biological investigations, different concentrations of GNP@P and GNS@P (0–100 μg mL^{-1}) were resuspended in complete media and exposed respectively to 532 nm laser at 1000 mW cm^{-2} and an 808 nm laser at 200 mW cm^{-2} for 15 min in order to assess the photothermal conversion of AuNPs (Fig. S1C and D). To exclude any potential interference, the 532 nm laser culture media (Euroclone) was used without phenol red. After assessing the photothermal capacity of the nanoparticles, they were placed in contact with the cells for 24 h to promote internalization (as described in section 4.8) and finally exposed to the laser to assess the viability (Fig. 7B and S7) and the apoptosis/necrosis death pathway (Fig. 7C, D and S8). The laser power densities used in this study (1 W cm^{-2} for GNPs and 200 mW cm^{-2} for GNSs) were selected based on preliminary optimization experiments. First, nanoparticles were exposed to different laser power settings to achieve temperature increases within the mild photothermal therapy range (42–45 °C), known to induce cell damage without harming surrounding healthy tissue. Second, our goal was to trigger effective photothermal responses while minimizing nonspecific thermal effects. When exposed to the same power with their respective laser wavelengths, GNS@P were able to absorb more light and produce greater heat than GNP@P, due to their enhanced optical absorption and plasmonic features in the near-infrared region. For this reason, after testing different power densities for GNPs, 1 W cm^{-2} was applied to GNP@P to reach a comparable therapeutic temperature range. What we realized was thus not exactly a normalization based on a measured absorption spectrum, but the compensation of the lower GNP@P absorp-

tion (with respect to GNS@P) so that an equivalent thermal effect was produced.

Viability assays. 12Z, HESC and NIH-3T3 cell lines were seeded on 48-well plates as described above, and then incubated with/without 24 μg mL^{-1} of Au@P_AbCD44 for 24 hours. Next, all the cells were washed three times with PBS to ensure the removal of the excess vectors from the solution, and then replaced with fresh medium before exposure to NIR laser light. The experimental conditions of each cell line were divided into two groups: cells incubated with GNP@P_AbCD44 were irradiated with a 532 nm laser at 1000 mW cm^{-2} for 15 min (due to the LSPR see Fig. 2A); cells treated with GNS@P_AbCD44 were irradiated with an 808 nm laser at 200 mW cm^{-2} for 15 min (due to the LSPR see Fig. 2B). Viability was assessed with Alamar blue assay (TOX8-Sigma Aldrich) after 24 and 48 h of irradiation, respectively. According to the protocol, 30 μL Alamar blue reagent was added in 300 μL of medium to each well, and all the cells were incubated at 37 °C for 4 hours. The cell viability was measured and expressed as a percentage related to the CTRL (untreated cells) set equal to 100%. Cells not incubated with Au@P_AbCD44 but exposed to laser did not show a reduction in cell viability.

Apoptosis and necrosis evaluation. 12Z cells seeded on 48-well plates as described above, and then incubated with/without 24 μg mL^{-1} of GNP@P_AbCD44 and GNS@P_AbCD44 for 24 hours, respectively. Next, all the cells were washed three times with PBS, added with culture media and exposed to laser. Finally, the cells were stained using a Necrosis/apoptosis kit (Abcam ab176749) and images acquired using a Thunder Imaging System (Leica Microsystems). The experimental conditions were divided into seven groups: untreated cells (no Au@P_AbCD44 and no laser exposure) (i), only laser treated cells (no Au@P_AbCD44) (ii), cells treated only with Au@P_AbCD44 (no laser exposure) (iii–iv), cells treated with Au@P_AbCD44, and laser exposed (v–vi). CTRL+ was induced by the addition of 1 μM staurosporine for 3 hours (vii). Fluorescent analysis shows 12Z cells that are alive (blue, stained with CytoCalcein Violet 450), apoptotic (green, Apopxin Green indicator), and necrotic (red, 7-AAD).[138,139]

To ensure quantitative robustness and reproducibility, apoptosis was assessed by analyzing five independent images acquired from five biologically distinct samples ($n = 5$). Quantification was performed using ImageJ, allowing for statistically supported comparisons across experimental groups. This approach provides reliable and reproducible data, as each quantified image represents an independent biological replicate.

4.10. Statistical analyses

Statistics regarding biological data was carried out by considering the mean of the results (in triplicate) obtained from three separate experiments ($n = 3$).

All statistical calculations were carried out using GraphPad Prism 9.3.1 (GraphPad Inc., San Diego, CA, United States). Statistical analysis was performed using Student's unpaired t-test and through one-way and two variance analysis (ANOVA),

followed by Bonferroni *post hoc*, for multiple comparisons (significance level of $p \leq 0.05$).

Author contributions

Conflicts of interest

There are no conflicts to declare

Data availability

The data supporting this article have been included as part of the SI.

The SI provides additional characterization data, and supporting figures that complement the main findings of the study. See DOI: https://doi.org/10.1039/d5bm00701a.

Acknowledgements

References

1 S. Ferrero, E. Arena, A. Morando and V. Remorgida, *Int. J. Gynecol. Obstet.*, 2010, **110**, 203–207.

2 M. Morotti, V. Remorgida, P. L. Venturini and S. Ferrero, *Arch. Gynecol. Obstet.*, 2012, **286**, 1571–1575.

3 L. M. Mikhaleva, V. E. Radzinsky, M. R. Orazov, T. N. Khovanskaya, A. V. Sorokina, S. A. Mikhalev, S. V. Volkova, V. B. Shustova and M. Y. Sinelnikov, *Int. J. Women's Health*, 2021, **13**, 525–537.

4 M. Terzic, G. Aimagambetova, J. Kunz, G. Bapayeva, B. Aitbayeva, S. Terzic and A. S. Laganà, *Int. J. Mol. Sci.*, 2021, **22**, 9274.

5 M. Zhao, M. Zhang, Q. Yu, W. Fei, T. Li, L. Zhu, Y. Yao, C. Zheng and X. Zhang, *Front. Bioeng. Biotechnol.*, 2022, **10**, 918368.

6 G. Tan, K. Kantner, Q. Zhang, M. Soliman, P. Del Pino, W. Parak, M. Onur, D. Valdeperez, J. Rejman and B. Pelaz, *Nanomaterials*, 2015, **5**, 1297–1316.

7 D. R. Matasariu, A. I. G. Bausic, C. E. Mandici, I. E. Bujor, A. E. Cristofor, E. Bratila, L. Lozneanu, L. V. Boiculese, M. Grigore and A. Ursache, *Biomedicines*, 2023, **11**, 2036.

8 A. Pazhohan, F. Amidi, F. Akbari-Asbagh, E. Seyedrezazadeh, Y. Aftabi, J. Abdolalizadeh, M. Khodarahmian, N. Khanlarkhani and A. Sobhani, *J. Steroid Biochem. Mol. Biol.*, 2018, **178**, 150–158.

9 L. Kiesel and M. Sourouni, *Climacteric*, 2019, **22**, 296–302.

10 P. R. Koninckx, R. Fernandes, A. Ussia, L. Schindler, A. Wattiez, S. Al-Suwaidi, B. Amro, B. Al-Maamari, Z. Hakim and M. Tahlak, *Front. Endocrinol.*, 2021, **12**, 745548.

11 C. B. Sieberg, C. E. Lunde and D. Borsook, *Neurosci. Biobehav. Rev.*, 2020, **108**, 866–876.

12 K. Shakiba, J. F. Bena, K. M. McGill, J. Minger and T. Falcone, *Obstet. Gynecol.*, 2008, **111**, 1285–1292.

13 U. Leone Roberti Maggiore, J. K. Gupta and S. Ferrero, *Eur. J. Obstet. Gynecol. Reprod. Biol.*, 2017, **209**, 81–85.

14 R. Zhang, F. Kiessling, T. Lammers and R. M. Pallares, *Drug Delivery Transl. Res.*, 2023, **13**, 378–385.

15 Y. Liu, B. M. Crawford and T. Vo-Dinh, *Immunotherapy*, 2018, **10**, 1175–1188.

16 W. Yang, H. Liang, S. Ma, D. Wang and J. Huang, *Sustainable Mater. Technol.*, 2019, **22**, e00109.

17 N. Gupta and R. Malviya, *Biochim. Biophys. Acta, Rev. Cancer*, 2021, **1875**, 188532.

18 H. Norouzi, K. Khoshgard and F. Akbarzadeh, *Lasers Med. Sci.*, 2018, **33**, 917–926.

19 L. F. A. Al-Barram, *Lasers Med. Sci.*, 2021, **36**, 325–337.

20 Z. Abed, J. Beik, S. Laurent, N. Eslahi, T. Khani, E. S. Davani, H. Ghaznavi and A. Shakeri-Zadeh, *J. Cancer Res. Clin. Oncol.*, 2019, **145**, 1213–1219.

21 M. M. Movahedi, A. Mehdizadeh, F. Koosha, N. Eslahi, V. P. Mahabadi, H. Ghaznavi and A. Shakeri-Zadeh, *Photodiagn. Photodyn. Ther.*, 2018, **24**, 324–331.

22 X. Huang and M. A. El-Sayed, *J. Adv. Res.*, 2010, **1**, 13–28.

23 L. Xing, D. Li, B. Chen, H. Gan and Y. Zhong, *Lasers Surg. Med.*, 2022, **54**, 433–446.

24 H. Moustaoui, J. Saber, I. Djeddi, Q. Liu, A. T. Diallo, J. Spadavecchia, M. Lamy De La Chapelle and N. Djaker, *J. Phys. Chem. C*, 2019, **123**, 17548–17554.

25 A. Pal, K. Esumi and T. Pal, *J. Colloid Interface Sci.*, 2005, **288**, 396–401.

26 M. Brust, M. Walker, D. Bethell, D. J. Schiffrin and R. Whyman, *J. Chem. Soc., Chem. Commun.*, 1994, 801–802.

27 J. G. Hinman, A. J. Stork, J. A. Varnell, A. A. Gewirth and C. J. Murphy, *Faraday Discuss.*, 2016, **191**, 9–33.

28 S. Kundu, L. Peng and H. Liang, *Inorg. Chem.*, 2008, **47**, 6344–6352.

29 S. J. Amina and B. Guo, *Int. J. Nanomedicine*, 2020, **15**, 9823–9857.

30 S. Zeng, K.-T. Yong, I. Roy, X.-Q. Dinh, X. Yu and F. Luan, *Plasmonics*, 2011, **6**, 491–506.

31 P. Christopher, H. Xin, A. Marimuthu and S. Linic, *Nat. Mater.*, 2012, **11**, 1044–1050.

32 R. A. Odion, Y. Liu and T. Vo-Dinh, *Cancers*, 2022, **14**, 5737.

33 Z. Xi, R. Zhang, F. Kiessling, T. Lammers and R. M. Pallares, *ACS Biomater. Sci. Eng.*, 2024, **10**, 38–50.

34 X. Wen, L. Ou, G. Cutshaw, S. Uthaman, Y. Ou, T. Zhu, S. Szakas, B. Carney, J. Houghton, A. Gundlach-Graham, M. Rafat, K. Yang and R. Bardhan, *Small*, 2023, **19**, 2204293.

35 W. Li and X. Chen, *Nanomedicine*, 2015, **10**, 299–320.

36 Y. Chen and X. Feng, *Int. J. Pharm.*, 2022, **625**, 122122.

37 P. Ghosh, G. Han, M. De, C. Kim and V. Rotello, *Adv. Drug Delivery Rev.*, 2008, **60**, 1307–1315.

38 H. Chen, X. Zhang, S. Dai, Y. Ma, S. Cui, S. Achilefu and Y. Gu, *Theranostics*, 2013, **3**, 633–649.

39 H.-C. Lin, K.-F. Hsu, C.-L. Lai, T.-C. Wu, H.-F. Chen and C.-H. Lai, *Molecules*, 2020, **25**, 1853.

40 R. Odion, Y. Liu and T. Vo-Dinh, *IEEE J. Sel. Top. Quantum Electron.*, 2021, **27**, 1–9.

41 L. Xing, B. Chen, D. Li, W. Wu and Z. Ying, *Lasers Surg. Med.*, 2018, **50**, 669–679.

42 J. Shao, R. J. Griffin, E. I. Galanzha, J.-W. Kim, N. Koonce, J. Webber, T. Mustafa, A. S. Biris, D. A. Nedosekin and V. P. Zharov, *Sci. Rep.*, 2013, **3**, 1293.

43 D. Pallarés-Aldeiturriaga, P. Roldán-Varona, L. Rodríguez-Cobo and J. M. López-Higuera, *Sensors*, 2020, **20**, 6971.

44 A. Gołąbek-Grenda and A. Olejnik, *Cell. Signalling*, 2022, **97**, 110375.

45 J. R. H. Wendel, X. Wang, L. J. Smith and S. M. Hawkins, *Biomedicines*, 2020, **8**, 525.

46 X.-F. Tang, H.-Y. Liu, L. Wu, M.-H. Li, S.-P. Li and H.-B. Xu, *Oncotarget*, 2017, **8**, 105703–105713.

47 J. Natesh, C. Chandola, S. M. Meeran and M. Neerathilingam, *Ther. Delivery*, 2021, **12**, 693–703.

48 J. C. Lee, N. D. Donahue, A. S. Mao, A. Karim, M. Komarneni, E. E. Thomas, E. R. Francek, W. Yang and S. Wilhelm, *ACS Appl. Nano Mater.*, 2020, **3**, 2421–2429.

49 D. Yadav and H. K. Dewangan, *J. Biomater. Sci., Polym. Ed.*, 2021, **32**, 266–280.

50 C. Von Baeckmann, H. Kählig, M. Lindén and F. Kleitz, *J. Colloid Interface Sci.*, 2021, **589**, 453–461.

51 C. Guo, H. Yuan, Y. Wang, Y. Feng, Y. Zhang, T. Yin, H. He, J. Gou and X. Tang, *Adv. Drug Delivery Rev.*, 2023, **200**, 115044.

52 N. Bloise, A. Massironi, C. Della Pina, J. Alongi, S. Siciliani, A. Manfredi, M. Biggiogera, M. Rossi, P. Ferruti, E. Ranucci and L. Visai, *Front. Bioeng. Biotechnol.*, 2020, **8**, 132.

53 M. H. Mohd-Zahid, S. Nurani Zulkifli, C. A. Che Abdullah, J. Lim, S. Fakurazi, K. K. Wong, A. D. Zakaria, N. Ismail, V. Uskoković, R. Mohamud and Z. A. Iskandar, *RSC Adv.*, 2021, **11**, 16131–16141.

54 M. Hasanzadeh Kafshgari, L. Agiotis, I. Largillière, S. Patskovsky and M. Meunier, *Small*, 2021, **17**, 2007577.

55 S. Liang, M. Sun, Y. Lu, S. Shi, Y. Yang, Y. Lin, C. Feng, J. Liu and C. Dong, *J. Mater. Chem. B*, 2020, **8**, 8368–8382.

56 T. Ji, M. C. Muenker, R. V. L. Papineni, J. W. Harder, D. L. Vizard and W. E. Mclaughlin, *Bioconjugate Chem.*, 2010, **21**, 427–435.

57 S. Miyagi, R. Yokoo, T. Tanigawa, D. B. Pitna, M. Hirose and T. Usuki, *Tetrahedron Lett.*, 2022, **90**, 153616.

58 X. Deng, M. Zeng, X. Wang, J. Liu, Y. Ma, X. Wang and L. Xu, *J. Chromatogr., A*, 2021, **1642**, 462000.

59 E. Van Bracht, S. Stolle, T. G. Hafmans, O. C. Boerman, E. Oosterwijk, T. H. Van Kuppevelt and W. F. Daamen, *Eur. J. Pharm. Biopharm.*, 2014, **87**, 80–89.

60 I. Steinhauser, B. Spänkuch, K. Strebhardt and K. Langer, *Biomaterials*, 2006, **27**, 4975–4983.

61 S. Wagner, F. Rothweiler, M. G. Anhorn, D. Sauer, I. Riemann, E. C. Weiss, A. Katsen-Globa, M. Michaelis, J. Cinatl, D. Schwartz, J. Kreuter, H. Von Briesen and K. Langer, *Biomaterials*, 2010, **31**, 2388–2398.

62 V. Sanfilippo, V. C. L. Caruso, L. M. Cucci, R. Inturri, S. Vaccaro and C. Satriano, *Int. J. Mol. Sci.*, 2020, **21**, 3085.

63 W.-Y. Huang, J.-N. Lin, J.-T. Hsieh, S.-C. Chou, C.-H. Lai, E.-J. Yun, U.-G. Lo, R.-C. Pong, J.-H. Lin and Y.-H. Lin, *ACS Appl. Mater. Interfaces*, 2016, **8**, 30722–30734.

64 D. Kalyane, S. Polaka, N. Vasdev and R. K. Tekade, *Pharmaceutics*, 2022, **14**, 2734.

65 C.-S. Lee, T. W. Kim, Y. Kang, Y. Ju, J. Ryu, H. Kong, Y.-S. Jang, D. E. Oh, S. J. Jang, H. Cho, S. Jeon, J. Kim and T. H. Kim, *Mater. Today Chem.*, 2022, **26**, 101083.

66 P. R. Rauta, P. M. Hallur and A. Chaubey, *Sci. Rep.*, 2018, **8**, 2893.

67 A. Yasin, Y. Ren, J. Li, Y. Sheng, C. Cao and K. Zhang, *Front. Bioeng. Biotechnol.*, 2022, **10**, 910290.

68 J. Kadkhoda, M. Akrami-Hasan-Kohal, M. R. Tohidkia, S. Khaledi, S. Davaran and A. Aghanejad, *Int. J. Biol. Macromol.*, 2021, **185**, 664–678.

69 Z. R. Goddard, M. J. Marín, D. A. Russell and M. Searcey, *Chem. Soc. Rev.*, 2020, **49**, 8774–8789.

70 W. Fei, X. Wang, J. Guo and C. Wang, *J. Mater. Chem. B*, 2023, **11**, 8228–8240.

71 L. Woythe, P. Madhikar, N. Feiner-Gracia, C. Storm and L. Albertazzi, *ACS Nano*, 2022, **16**, 3785–3796.

72 P. B. D. Silva, J. R. D. Silva, M. C. Rodrigues, J. A. Vieira, I. A. D. Andrade, T. Nagata, A. S. Santos, S. W. D. Silva, M. C. O. D. Rocha, S. N. Báo, P. M. Moraes-Vieira, J. Proença-Modena, M. K. C. Angelim, G. F. De Souza, S. P. Muraro, A. L. B. De Barros, G. A. De Souza Martins, F. Ribeiro-Dias, G. Machado, M. R. Fessel, A. M. Chudzinski-Tavassi, C. M. Ronconi, D. Gonçalves, R. Curi, O. N. Oliveira and R. B. Azevedo, *Talanta*, 2022, **243**, 123355.

73 J. Liu, J. Li, S. Zhang, M. Ding, N. Yu, J. Li, X. Wang and Z. Li, *Nano Convergence*, 2022, **9**, 13.

74 M. H. Jazayeri, T. Aghaie, R. Nedaeinia, M. Manian and H. Nickho, *Cancer Immunol. Immunother.*, 2020, **69**, 1833–1840.

75 Y. H. Lai, S. Koo, S. H. Oh, E. A. Driskell and J. D. Driskell, *Anal. Methods*, 2015, **7**, 7249–7255.

76 A. J. Miles, R. W. Janes and B. A. Wallace, *Chem. Soc. Rev.*, 2021, **50**, 8400–8413.

77 L. Minati, F. Benetti, A. Chiappini and G. Speranza, *Colloids Surf., A*, 2014, **441**, 623–628.

78 G. P. Sahoo, H. Bar, D. K. Bhui, P. Sarkar, S. Samanta, S. Pyne, S. Ash and A. Misra, *Colloids Surf., A*, 2011, **375**, 30–34.

79 B. Bassi, G. Dacarro, P. Galinetto, E. Giulotto, N. Marchesi, P. Pallavicini, A. Pascale, S. Perversi and A. Taglietti, *Nanotechnology*, 2018, **29**, 235301.

80 B. Bassi, B. Albini, A. D'Agostino, G. Dacarro, P. Pallavicini, P. Galinetto and A. Taglietti, *Nanotechnology*, 2019, **30**, 025302.

81 I. Ettah and L. Ashton, *Antibodies*, 2018, **7**, 24.

82 S. Schlücker, *ChemPhysChem*, 2009, **10**, 1344–1354.

83 M. M. Joseph, N. Narayanan, J. B. Nair, V. Karunakaran, A. N. Ramya, P. T. Sujai, G. Saranya, J. S. Arya, V. M. Vijayan and K. K. Maiti, *Biomaterials*, 2018, **181**, 140–181.

84 D. Kumar, I. Mutreja, K. Chitcholtan and P. Sykes, *Nanotechnology*, 2017, **28**, 475101.

85 P. J. Chueh, R.-Y. Liang, Y.-H. Lee, Z.-M. Zeng and S.-M. Chuang, *J. Hazard. Mater.*, 2014, **264**, 303–312.

86 A. Kumar, N. Das and R. G. Rayavarapu, *J. Nanotheranostics*, 2023, **4**, 1–34.

87 A. Sani, C. Cao and D. Cui, *Biochem. Biophys. Rep.*, 2021, **26**, 100991.

88 A. Juan, F. J. Cimas, I. Bravo, A. Pandiella, A. Ocaña and C. Alonso-Moreno, *Int. J. Mol. Sci.*, 2020, **21**, 6018.

89 M. Kumari, A. Acharya and P. T. Krishnamurthy, *Beilstein J. Nanotechnol.*, 2023, **14**, 912–926.

90 B. Yameen, W. I. Choi, C. Vilos, A. Swami, J. Shi and O. C. Farokhzad, *J. Controlled Release*, 2014, **190**, 485–499.

91 R. S. Riley and E. S. Day, *Wiley Interdiscip. Rev.: Nanomed. Nanobiotechnol.*, 2017, **9**, e1449.

92 D. M. Glatt, D. R. Beckford Vera, M. C. Parrott, J. C. Luft, S. R. Benhabbour and R. J. Mumper, *Mol. Pharmaceutics*, 2016, **13**, 1894–1903.

93 P. Nativo, I. A. Prior and M. Brust, *ACS Nano*, 2008, **2**, 1639–1644.

94 D. Huang, Y. Tan, J. Tang, K. He, Y. Zhou and J. Liu, *Angew. Chem., Int. Ed.*, 2024, **63**, e202316900.

95 R. Gonzalez-Pastor, Y. Hernandez, M. Gimeno, A. De Martino, Y. K. S. Man, G. Hallden, M. Quintanilla, J. M. De La Fuente and P. Martin-Duque, *Acta Biomater.*, 2021, **134**, 593–604.

96 X. P. Lin, J. D. Mintern and P. A. Gleeson, *Membranes*, 2020, **10**, 177.

97 C. T. Ng, F. M. A. Tang, J. J. Li, C. Ong, L. L. Y. Yung and B. H. Bay, *Anat. Rec.*, 2015, **298**, 418–427.

98 L. Pelkmans and A. Helenius, *Traffic*, 2002, **3**, 311–320.

99 B. Dutta, K. C. Barick and P. A. Hassan, *Adv. Colloid Interface Sci.*, 2021, **296**, 102509.

100 M. A. Dheyab, A. A. Aziz, P. M. Khaniabadi, M. S. Jameel, N. Oladzadabbasabadi, A. A. Rahman, F. S. Braim and B. Mehrdel, *Photodiagn. Photodyn. Ther.*, 2023, **42**, 103312.

101 A. S. Moses, O. R. Taratula, H. Lee, F. Luo, T. Grenz, T. Korzun, A. S. Lorenz, F. Y. Sabei, S. Bracha, A. W. G. Alani, O. D. Slayden and O. Taratula, *Small*, 2020, **16**, 1906936.

102 X. Liu, S. Yan, H. Wu, M. Chen, H. Dai, Z. Wang, M. Chai, Q. Hu, D. Li, L. Chen, R. Diao, S. Chen, L. Wang and X. Shi, *Adv. Funct. Mater.*, 2024, **34**, 2315907.

103 X. Guo, W. Li, J. Zhou, W. Hou, X. Wen, H. Zhang, F. Kong, L. Luo, Q. Li, Y. Du and J. You, *Small*, 2017, **13**, 1603270.

104 L.-R. Rau, S.-W. Tsao, J.-W. Liaw and S.-W. Tsai, *Biomacromolecules*, 2016, **17**, 2514–2521.

105 H. Villuendas, C. Vilches and R. Quidant, *ACS Nanosci. Au*, 2023, **3**, 347–352.

106 J. R. Melamed, R. S. Edelstein and E. S. Day, *ACS Nano*, 2015, **9**, 6–11.

107 M. Pérez-Hernández, P. Del Pino, S. G. Mitchell, M. Moros, G. Stepien, B. Pelaz, W. J. Parak, E. M. Gálvez, J. Pardo and J. M. De La Fuente, *ACS Nano*, 2015, **9**, 52–61.

108 H. He, C. Xie and J. Ren, *Anal. Chem.*, 2008, **80**, 5951–5957.

109 T. Ilovitsh, Y. Danan, R. Meir, A. Meiri and Z. Zalevsky, *Sci. Rep.*, 2015, **5**, 8244.

110 M. T. Spencer, H. Furutani, S. J. Oldenburg, T. K. Darlington and K. A. Prather, *J. Phys. Chem. C*, 2008, **112**, 4083–4090.

111 H. Ye, Y. Liu, L. Zhan, Y. Liu and Z. Qin, *Theranostics*, 2020, **10**, 4359–4373.

112 Z. Qin, W. C. W. Chan, D. R. Boulware, T. Akkin, E. K. Butler and J. C. Bischof, *Angew. Chem., Int. Ed.*, 2012, **51**, 4358–4361.

113 N. Kumar, M. A. Sadique, R. Khan, V. S. Gowri, S. Kumar, M. Ashiq and S. Natarajan, *Hybrid Adv.*, 2023, **3**, 100065.

114 P. Ranjan, M. Abubakar Sadique, S. Yadav and R. Khan, *ACS Appl. Mater. Interfaces*, 2022, **14**, 20802–20812.

115 A. Bekmurzayeva, Z. Ashikbayeva, Z. Myrkhiyeva, A. Nugmanova, M. Shaimerdenova, T. Ayupova and D. Tosi, *Sci. Rep.*, 2021, **11**, 19583.

116 V. Voliani, G. Signore, O. Vittorio, P. Faraci, S. Luin, J. Peréz-Prieto and F. Beltram, *J. Mater. Chem. B*, 2013, **1**, 4225.

117 C. Song, F. Li, X. Guo, W. Chen, C. Dong, J. Zhang, J. Zhang and L. Wang, *J. Mater. Chem. B*, 2019, **7**, 2001–2008.

118 T. Vo-Dinh, *J. Immunol. Sci.*, 2018, **2**, 1–8.

119 J. F. Knudtson, J. E. McLaughlin, M. Tellez Santos, P. Binkley, S. Reddy, R. Tekmal and R. S. Schenken, *Fertil. Steril.*, 2018, **110**, e390.

120 R. Paravati, N. De Mello, E. K. Onyido, L. W. Francis, K. Brüsehafer, K. Younas, S. Spencer-Harty, R. S. Conlan, D. Gonzalez and L. Margarit, *J. Mol. Med.*, 2020, **98**, 1713–1725.

121 S. D. Fontaine, R. Reid, L. Robinson, G. W. Ashley and D. V. Santi, *Bioconjugate Chem.*, 2015, **26**, 145–152.

122 W. Huang, X. Wu, X. Gao, Y. Yu, H. Lei, Z. Zhu, Y. Shi, Y. Chen, M. Qin, W. Wang and Y. Cao, *Nat. Chem.*, 2019, **11**, 310–319.

123 A. S. C. Gonçalves, C. F. Rodrigues, A. F. Moreira and I. J. Correia, *Acta Biomater.*, 2020, **116**, 105–137.

124 G. Chirico, M. Borzenkov and P. Pallavicini, *Gold Nanostars: Synthesis, Properties and Biomedical Application*, Springer International Publishing, Cham, 2015.

125 P. Pallavicini, L. De Vita, F. Merlin, C. Milanese, M. Borzenkov, A. Taglietti and G. Chirico, *Molecules*, 2020, **25**, 2499.

126 M. Okkeh, L. De Vita, G. Bruni, L. Doveri, P. Minzioni, E. Restivo, M. Patrini, P. Pallavicini and L. Visai, *RSC Adv.*, 2023, **13**, 33887–33904.

127 A. Casu, E. Cabrini, A. Donà, A. Falqui, Y. Diaz-Fernandez, C. Milanese, A. Taglietti and P. Pallavicini, *Chem. – Eur. J.*, 2012, **18**, 9381–9390.

128 A. C. Marques, P. J. Costa, S. Velho and M. H. Amaral, *J. Controlled Release*, 2020, **320**, 180–200.

129 C. K. Riener, G. Kada and H. J. Gruber, *Anal. Bioanal. Chem.*, 2002, **373**, 266–276.

130 R. J. Simpson, *Cold Spring Harbor Protoc.*, 2008, **2008**, 4722.

131 L. Martínez-Jothar, N. Beztsinna, C. F. Van Nostrum, W. E. Hennink and S. Oliveira, *Mol. Pharmaceutics*, 2019, **16**, 1633–1647.

132 O. T. Marişca and N. Leopold, *Materials*, 2019, **12**, 1131.

133 K. A. Kang, J. Wang, J. B. Jasinski and S. Achilefu, *J. Nanobiotechnol.*, 2011, **9**, 16.

134 N. El-Sayed, K. Elbadri, A. Correia and H. A. Santos, *Adv. Mater. Technol.*, 2023, **8**, 2301159.

135 A. A. H. Abdellatif and H. M. Tawfeek, *Drug Dev. Ind. Pharm.*, 2018, **44**, 1679–1684.

136 N. Gunduz, H. Ceylan, M. O. Guler and A. B. Tekinay, *Sci. Rep.*, 2017, **7**, 40493.

137 C. Casali, S. Siciliani, L. Galgano and M. Biggiogera, *Int. J. Mol. Sci.*, 2023, **24**, 153, DOI: **10.3390/ijms24010153**.

138 C. E. Maurici, R. Colenbier, B. Wylleman, L. Brancato, E. Van Zwol, J. Van Den Bossche, J.-P. Timmermans, E. Giovannetti, M. G. M. C. Mori Da Cunha and J. Bogers, *Biomolecules*, 2022, **12**, 651.

139 T. M. Le, N. Morimoto, N. T. M. Ly, T. Mitsui, S. C. Notodihardjo, S. Ogino, J. Arata, N. Kakudo and K. Kusumoto, *Stem Cell Rev. Rep.*, 2021, **17**, 662–672.